https://doi.org/10.5194/egusphere-2026-842
Preprint. Discussion started: 24 February 2026

Characteristics of marine aerosols and cloud condensation nuclei measured during the cruise of R/V *ISABU* in 2024: from the East China Sea to the Indian Ocean

Chanwoo Ahn[1, 2], Andrew Loh[3], Najin Kim[2], Un Hyuk Yim[3, 4], Joon Geon An[3], Kyung Hwan Kim[2], Donghwi Kim[3], Do-Hyeon Park[2], Seong Soo Yum[1, 2], Sun Choi[2]

[1]Department of Atmospheric Sciences, Yonsei University, Seoul, 03722, Republic of Korea

[2]Climate and Environmental Research Institute, Korea Institute of Science and Technology, Seoul, 02792, Republic of Korea

[3]Ecological Risk Research Department, Korea Institute of Ocean Science and Technology, Geoje, 53201, Republic of Korea

[4]KIOST School, University of Science and Technology, Busan, 49111, Republic of Korea

Correspondence to: Seong Soo Yum (ssyum@kist.re.kr)

https://doi.org/10.5194/egusphere-2026-842
Preprint. Discussion started: 24 February 2026

Abstract. Marine aerosols and cloud condensation nuclei (CCN) exhibit significant spatial variability over the global ocean, but observational constraints remain limited by short-term or regionally confined measurements. This study offers a comprehensive examination of marine aerosols and CCN characteristics across the East China Sea, the South China Sea, the Strait of Malacca, and the Indian Ocean, based on continuous ship measurements during the transit voyage of the R/V *ISABU* in 2024. By applying a consistent observational and analytical framework, various characteristics were intercompared across different sea areas. Aerosol and CCN number concentrations varied by more than two orders of magnitude, with clear contrasts between continent-adjacent seas and the remote ocean. The Indian Ocean represented a clean marine background characterized by low aerosol number concentrations but high hygroscopicity. In contrast, a distinct volcanic-influence episode over the South China Sea exhibited exceptionally elevated CCN number concentrations. Differences in aerosol size distributions and hygroscopicity resulted in substantial regional variability in CCN activation. Furthermore, cluster analysis demonstrated that marine-origin air masses consistently possess a higher activation efficiency than continental ones. These findings emphasize that the complex interactions among aerosol number concentration, size distribution, and hygroscopicity govern marine CCN characteristics, providing essential constraints for refining parameterizations of aerosol–cloud interactions in climate models.

https://doi.org/10.5194/egusphere-2026-842
Preprint. Discussion started: 24 February 2026

1. Introduction

Atmospheric aerosols are a key factor contributing to uncertainties in climate prediction (Carslaw et al., 2013; Bellouin et al., 2020). They have a direct impact on the Earth's radiation balance by absorbing and scattering solar radiation (Twomey, 1991; Haywood and Boucher, 2000). In addition, aerosols can act as cloud condensation nuclei (CCN), affecting cloud droplet size, albedo, cloud lifetime, and precipitation efficiency (Twomey, 1974; Albrecht, 1989). As a result, the radiative properties of clouds are indirectly altered by aerosols—an effect highlighted as a significant source of uncertainty in recent studies (Park et al., 2025; Kumar and Tiwari, 2026). The IPCC Sixth Assessment Report estimated the total radiative forcing from aerosols, integrating aerosol–radiation and aerosol–cloud interactions, to be $-1.1\ W\ m^{-2}$ (-1.7 to -0.4) (Forster et al., 2021). This value roughly offsets about half of the forcing induced by CO_2, a representative greenhouse gas ($2.16\ W\ m^{-2}$, 1.9 to 2.41). However, the same assessment simultaneously highlighted that the cooling effect of aerosols remains the crucial source of uncertainty. Chen et al. (2024) further emphasized that this uncertainty is particularly pronounced over the ocean, where extensive low-cloud coverage complicates quantitative assessments of aerosol–cloud interactions.

Marine aerosols originate from a variety of sources. Sea salt, a primary natural component, is mainly generated by bubble bursting (Lewis and Schwartz, 2004) and wave breaking (Monahan et al., 1986). Marine organic matter can likewise be emitted into the atmosphere from the ocean through the same process (O'Dowd and de Leeuw, 2007; Quinn and Bates, 2011). Another natural component is non-sea salt sulfate (nss-sulfate). Dimethyl sulfide (DMS), which is emitted by marine phytoplankton, is the dominant reduced sulfur compound in the marine atmosphere and subsequently forms nss-sulfate through oxidation and gas-to-particle conversion (Andreae and Crutzen, 1997; Quinn et al., 2023). Terrestrial aerosols can also become major marine aerosol constituents when they are transported to oceanic areas. In marine areas adjacent to the polluted East Asian region (e.g., the East China Sea and Yellow Sea), anthropogenic aerosols such as sulfate, nitrate, and black carbon are dominant (Yoo et al., 2025; Zhou et al., 2025). Mineral dust originating from deserts exerts a substantial influence on the northern Indian Ocean, particularly over the Arabian Sea (Moorthy et al., 2005; Aswini et al., 2022). In addition to marine and terrestrial sources, ship exhaust from fuel combustion can also be an important aerosol source in heavily trafficked shipping lanes such as the South China Sea and the Strait of Malacca (Thornton et al., 2017; Miller et al., 2023).

https://doi.org/10.5194/egusphere-2026-842
Preprint. Discussion started: 24 February 2026

The diverse origins of marine aerosols significantly influence aerosol size distribution, hygroscopicity (κ), and CCN activity. Sea salt primarily consists of accumulation and coarse mode particles with high κ, enabling them to readily act as CCN under most atmospheric conditions (King et al., 2012; Gaston et al., 2018). Sulfate aerosols are predominantly found in the Aitken and accumulation mode; due to their relatively high κ, a large fraction of these aerosols can be activated as CCN (Sanchez et al., 2018; Park et al., 2021). Organic aerosols, which are typically less hygroscopic, can induce large variations in CCN number concentrations (N_{CCN}) depending on their relative abundance (Martin et al., 2011; Coggon et al., 2014). As such, even modest changes in marine aerosol characteristics can significantly alter CCN activity, ultimately modifying the properties of marine low-level clouds like stratocumulus and shallow cumulus clouds (Wood et al., 2015; Fan et al., 2016). Therefore, aerosol–cloud interactions over the ocean remain a key contributor to climate prediction uncertainty, underscoring the need for long-term, spatially extensive observations of aerosols and CCN.

In an effort to better characterize marine aerosols and CCN, ship-based observations have been conducted in various oceanic regions. The following are some examples of Northern Hemisphere measurements. Park et al. (2020) reported that N_{CCN} at 0.4% supersaturation (SS) during a cruise from the Arctic Ocean to the Pacific Ocean were only 35 ± 40 cm^{-3} in Arctic marine air masses, increased to 71 ± 47 cm^{-3} in Arctic terrestrial inflow, and reached 204 ± 87 cm^{-3} in the Pacific Ocean. Gong et al. (2023) reported CN (condensation nuclei, total aerosols) number concentrations (N_{CN}) and N_{CCN} at 0.4% SS of 5200 ± 3200 cm^{-3} and 1200 ± 750 cm^{-3}, respectively, from ship measurements across the East China Sea–Yellow Sea–Bohai Sea. The average value of κ was 0.36 ± 0.21, excluding abnormally low κ values (<0.1). Ou et al. (2025) conducted two ship measurements in the South China Sea. In the summer, when the sea was influenced by terrestrial outflow from Luzon and Indochina, Aitken mode particle concentrations, κ, and CCN activation ratios (N_{CCN}/N_{CN}) were elevated. In contrast, during the winter, air masses were dominantly influenced by East Asia and exhibited reduced κ for small particles, resulting in lower N_{CCN}/N_{CN} ratios. Nair et al. (2020) investigated continental influence over the northern Indian Ocean during winter using ship measurements. Under polluted continental air masses, N_{CCN} at 0.4–0.6% SS frequently exceeded 5000 cm^{-3}, and the N_{CCN}/N_{CN} ratios were markedly low (~0.25). Near the equator, however, N_{CCN} were around 1000 cm^{-3} and N_{CCN}/N_{CN} ratios were much higher.

https://doi.org/10.5194/egusphere-2026-842
Preprint. Discussion started: 24 February 2026

Meanwhile, the following are examples of Southern Hemisphere measurements. Dournaux et al. (2025) reported from recent long-term ship measurements in the southwestern Indian Ocean that submicron N_{CN} ranged widely from ~100 to over 3000 cm^{-3}. However, N_{CCN} at 0.4% SS were more constrained, ranging from 60 to 500 cm^{-3}, and κ values varied from 0.05 to 0.7, depending on the origin of the air masses. Sanchez et al. (2021), during a round trip between Tasmania and 62°S, showed that N_{CCN} increased near the coasts of Australia and Antarctica, while the minimum concentration occurred in the midlatitude storm belt due to precipitation scavenging. They observed that κ values were higher at lower latitudes due to a greater proportion of sea salt. In contrast, at higher latitudes, κ values were lower, associated with increased organic aerosol contributions. Tatzelt et al. (2022), using circum-Antarctic ship measurements, reported that N_{CCN} at 0.3% SS varied from 3 to 590 cm^{-3}. The κ values typically ranged from 0.2 to 0.9, indicating a broad spectrum of aerosol types, from organic-dominated to inorganic-dominated.

As summarized above, ship measurements conducted across the global ocean consistently demonstrate that N_{CCN} in the marine boundary layer typically span roughly two orders of magnitude, from several tens to thousands per cubic centimeter, and that κ values vary significantly depending on the dominant aerosol components. These studies also confirmed that such variability is strongly linked to sea area, season, and the origin of air masses. However, most measurements have been limited to short-term campaigns focused on a specific sea area or a single ocean, and very few studies—such as Flores et al. (2020)—have examined diverse oceanic environments continuously using a single platform. This limitation makes it difficult to assess differences in aerosol and CCN characteristics across various sea areas and to evaluate variability associated with changes in sources from a unified perspective.

To address these gaps, this study presents continuous, simultaneous observations of aerosols and CCN across the East China Sea, the South China Sea, the Strait of Malacca, and the Indian Ocean during long-distance transit voyages of the research vessel *ISABU* in 2024. We comprehensively compared the characteristics of aerosols and CCN across the four regions, including aerosol size distribution, activation efficiency, κ, and CCN spectra, all derived using a consistent methodology. In addition, by analyzing the origins of air masses and aerosol sources, we systematically interpreted the regional variability in CCN characteristics. Finally, we discuss the similarities and differences between the characteristics observed in this study and those reported in previous research.

https://doi.org/10.5194/egusphere-2026-842
Preprint. Discussion started: 24 February 2026

2. Methods

2.1. Overview of the campaign and measurement

2.1.1. Campaign information

In 2024, the Korea Institute of Ocean Science and Technology (KIOST) and the Korea Institute of Science and Technology (KIST) conducted joint comprehensive marine atmospheric observations onboard the R/V *ISABU* with a gross tonnage of 5894 tons, a length of 99.8 m, and a width of 18.0 m (Fig. 1). The primary objective of this campaign was to jointly investigate interactions among marine biology, marine atmosphere, cloud formation, and climate change. This was achieved through simultaneous measurements of marine aerosols, CCN, ice-nucleating particles (INP), and gaseous species, as well as in situ observations of atmospheric photochemical processes.

The transit voyage departed from Jangmok Port (34.993°N, 128.676°E) in Geoje, Republic of Korea, on March 28 and arrived in Port Louis (20.152°S, 57.494°E), Mauritius, on April 17, passing through the East China Sea, the South China Sea, the Strait of Malacca, and the Indian Ocean. The detailed cruise route and schedule are presented in Figure 2 and Table S1. The fact that measurements were conducted across diverse sea areas demonstrates the strength of this campaign, enabling consistent comparisons of regional characteristics.

https://doi.org/10.5194/egusphere-2026-842
Preprint. Discussion started: 24 February 2026

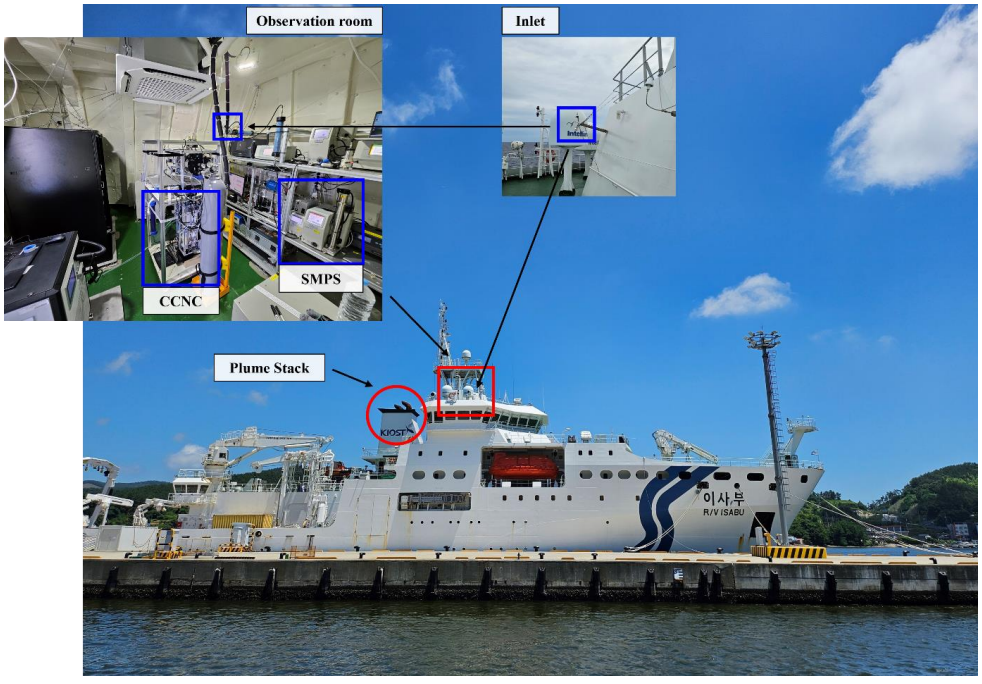

147

148 **Figure 1.** Picture of R/V *ISABU*. The red rectangle denotes the observation room with inlets,
149 and the four blue rectangles in the interior photograph indicate the SMPS, CCNC, and inlets.
150 The red circle represents the vessel's plume stack.

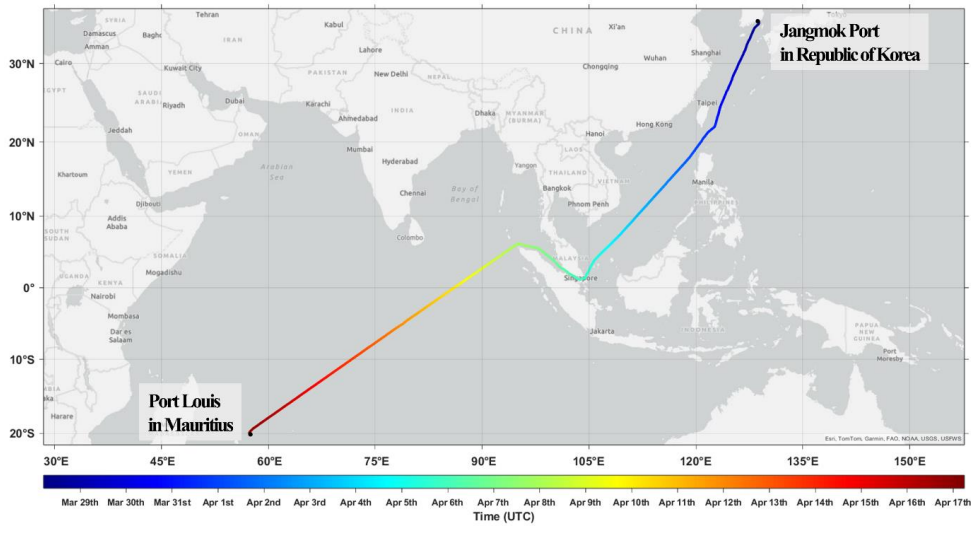

151

152 **Figure 2.** Cruise route of the R/V *ISABU* in 2024 (Source: Esri, TomTom, Garmin, FAO,
153 NOAA, USGS, USFWS; Powered by Esri).

https://doi.org/10.5194/egusphere-2026-842
Preprint. Discussion started: 24 February 2026

2.1.2. Measurement instruments

During the transit voyage of the R/V *ISABU*, various instruments were installed to measure both particulate and gaseous components in the atmosphere, as shown in Figure 1. The observation room was located on the uppermost F-deck (approximately 20 m above sea level) to minimize the influences of sea-salt particles and ammonia emitted by the vessel. All aerosol observation instruments were connected via a conductive tube to reduce losses. To limit the effects of high ambient humidity, a diffusion dryer was installed upstream of each instrument inlet. Nevertheless, due to the substantial temperature difference between the room and the outside, condensation occasionally occurred inside the tube, requiring periodic checks and the removal of water.

Among the various instruments, a scanning mobility particle sizer (SMPS; model 3938L89, TSI Inc., USA) and a cloud condensation nuclei counter (CCNC; model CCN-200, Droplet Measurement Technologies, USA) were used in this study. SMPS, which consists of an electrostatic classifier (Model 3082, TSI Inc., USA) and a condensation particle counter (CPC; model 3750, TSI Inc., USA), measured the aerosol size distribution every 3 minutes. The measured aerosol size range was 10.6–478.3 nm, divided into 107 bins. However, occasional voltage instabilities occurred at the smallest size bins, so the 10.6–14.6 nm range was excluded when calculating N_{CN}.

CCNC measured N_{CCN} at a given supersaturation every second. Although the CCNC model used in this study consisted of two columns, only one column was operated during the campaign due to a flow issue caused by a Nafion tube in one of the two columns. CCNC was set to run at supersaturations ranging from 0.2% to 1.0%, with increments of 0.2%. The measurement durations were 12 minutes for 0.2% SS and 5 minutes for the 0.4–1.0% SS. Thus, the nominal total measurement cycle of CCNC was 32 minutes. However, the instrument software did not initiate measurements at the next supersaturation immediately after completing the previous one. That is, the measurement timer began only after the temperature gradient between the top and bottom of the column reached the set value for the next supersaturation. As a result, the actual total measurement cycle during the cruise was approximately 50 minutes.

Furthermore, the time required for temperature stabilization varied even at the same supersaturation. Therefore, for efficient data processing, we uniformly excluded the first 15

https://doi.org/10.5194/egusphere-2026-842
Preprint. Discussion started: 24 February 2026

minutes of data at 0.2% SS and the first 3 minutes of data at the other supersaturations, regardless of the actual measurement start time. The relatively longer exclusion period for 0.2% SS was due to the substantial change in supersaturation from 1.0% to 0.2%. Unlike other changes, which took about 90 seconds to stabilize the temperature, this specific change required about 10 minutes. To ensure accurate measurements, we performed CCNC flow calibration and supersaturation calibration using $(NH_4)_2SO_4$ before and after the campaign.

2.2 Data processing

2.2.1. Quality control

To ensure reliable measurement data and to enable a consistent comparison across the different sea areas, we conducted data quality control following the procedure described below.

First, since the plume stack was located relatively behind the observation room, measurements might be contaminated by the vessel's exhaust when the wind blew rapidly from the stern (Fig. 3a). Therefore, data were excluded when the relative wind direction was between 150° and 270°, considering the relative positions of the inlet and plume stack. Fortunately, the wind blew from the bow during most of the cruise, and contamination by exhaust was minimal (Fig. 3b).

Second, temporary contamination could also occur due to ship maintenance activities such as painting and cleaning, cooking on board, or exhaust plumes from nearby ships (particularly in the Strait of Malacca). Such contamination was removed through a spike check. Using a 24-hour moving window, any data point that deviated from the median by more than 3 times the scaled Median Absolute Deviation (MAD) was considered an outlier and excluded from the dataset.

Lastly, we corrected the SMPS data. Due to an unidentified issue, likely related to relative humidity, N_{CN} occasionally exhibited a nearly order-of-magnitude change while maintaining a consistent size distribution (Fig. S1). Consequently, anomalous SMPS data were identified and corrected through comparison with the aerosol size distribution measured by the Aerodynamic Particle Sizer (APS). The corrected data were then validated against PM_1 data measured by the Aerosol Mass Spectrometer (AMS) and $PM_{2.5}$ data obtained by the beta attenuation method

https://doi.org/10.5194/egusphere-2026-842
Preprint. Discussion started: 24 February 2026

214 before being used for this study (Fig. S2). Details of the correction procedure are provided in
215 the Supplement (Sect. S1).

216 After applying these three procedures (including the exclusion mentioned in Section 2.1.2
217 for the CCNC), 86.8% of the SMPS data and 36.6% of the CCNC data were used for analysis,
218 which correspond to approximately 17.4 days and 7.33 days of data, respectively.

219

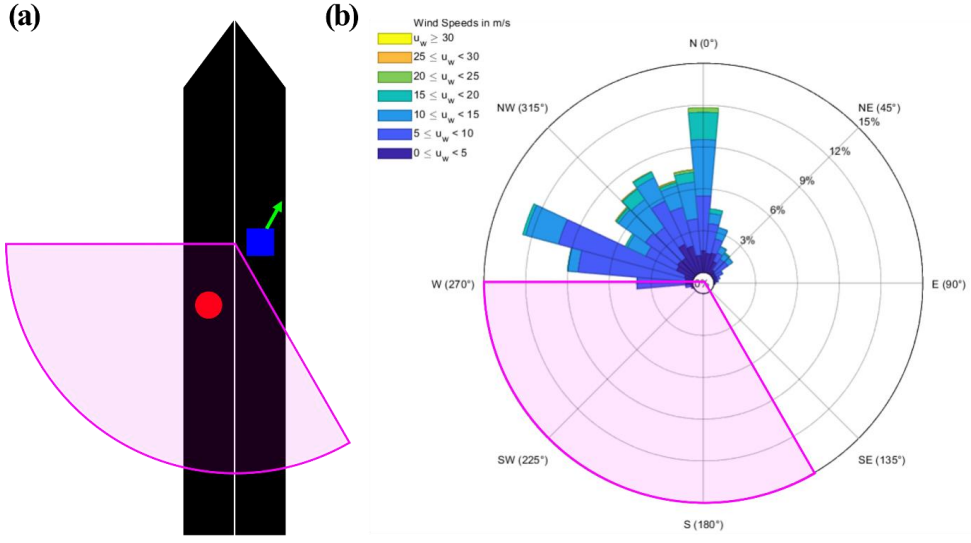

220

221 **Figure 3.** (a) Schematic diagram of the observation room and plume stack, and (b) relative
222 wind rose plot during the transit voyage of the R/V *ISABU*. The red circle, blue square, and
223 green arrow represent the plume stack, observation room, and the direction of inlets,
224 respectively. The magenta circular sector indicates a range from 150° to 270°.

225

226 *2.2.2. Critical diameter and hygroscopic parameter*

227 To calculate the critical diameter (D_C) at each supersaturation, we assumed that the aerosols
228 were internally mixed and that larger aerosols would be preferentially activated due to smaller
229 curvature effects. First, N_{CCN}, originally recorded at 1 s intervals, were averaged to match the
230 3-minute sampling interval of the SMPS. Then, N_{CN} from the largest to smallest diameter bins
231 of the observed size distribution were cumulatively summed. As explained in Eq. (1), the
232 diameter of the bin where the cumulative N_{CN} first exceeded the N_{CCN} was taken as D_C.

https://doi.org/10.5194/egusphere-2026-842
Preprint. Discussion started: 24 February 2026

$$N_{CCN} < \int_{D_C}^{478.3\ nm} N_{CN}(D_p) dD_p\ , \quad (1)$$

Hygroscopicity parameter (κ) represents the relationship between dry diameter and CCN activity and was calculated according to Petters and Kreidenweis (2007):

$$\kappa = \frac{4A^3}{27 D_c^3 \ln^2 S_c},\ A = \frac{4\sigma_{s/a} M_w}{RT\rho_w}, \quad (2)$$

where $\sigma_{s/a}$ is the surface tension of the solution/air interface, and in this study, it was assumed to be $0.072\ J\ m^{-2}$, corresponding to the surface tension of pure water. $M_w = 0.018\ kg\ mol^{-1}$ and $\rho_w = 997\ kg\ m^{-3}$ $(at\ 273.15\ K)$ are the molar mass and density of water, respectively. $R = 8.3145\ J\ mol^{-1}K^{-1}$ is the universal gas constant. T is the temperature; in this study, the measured temperature was used. S_c refers to the supersaturation used in the calculation of the corresponding D_c.

2.2.3. Back-trajectories and clustering analysis

To identify the origin and transport pathway of air masses during the cruise, back trajectories at 100 m altitude were calculated using the Hybrid Single-Particle Lagrangian Integrated Trajectory (HYSPLIT) model (Stein et al., 2015). For these calculations, the coordinates of the research vessel at each hour were used as the starting location. The total run time was set to 72 hours by default, but was extended to 120 hours when additional analysis was required. The meteorological input for HYSPLIT was sourced from the Global Data Assimilation System (GDAS) model with a 1° × 1° horizontal resolution.

To classify the origins of air masses over each sea area, k-means clustering analysis was conducted using the collected back-trajectory dataset. Fundamentally, clustering analysis requires all trajectories to share an identical starting location. However, because the starting locations of the acquired trajectories differed, the three-step preprocessing procedure (translation, vectorization, and standardization) was applied, as explained in detail in the Supplement (Sect. S2). The k-means clustering performed after this preprocessing had a limitation that it does not fully retain the actual geographic information of the trajectories. Therefore, while the k-means clustering results served as the primary basis, the geographic information of the original trajectories was additionally taken into account to finalize the classification.

https://doi.org/10.5194/egusphere-2026-842
Preprint. Discussion started: 24 February 2026

3. Results and discussions

3.1. Variations of aerosols and CCN

3.1.1. Spatiotemporal variability

Figure 4 presents the time series of aerosol size distribution (Fig. 4a), N_{CN} and N_{CCN} (Fig. 4b), temperature and relative humidity (RH) (Fig. 4c), true wind speed and direction (Fig. 4d), and precipitation and pressure (Fig. 4e) during the transit voyage of the R/V *ISABU*. Since the local time zone was adjusted five times in total (from UTC+9 to UTC+4), the Coordinated Universal Time (UTC) is shown in black along the bottom x-axis, and the Local Time (LT) is shown in gray along the top x-axis. The defined areas for each sea region are presented in Figure S3.

N_{CN} ranged from 11 to 9171 cm^{-3}, with an average of 695 ± 889 cm^{-3}, and exhibited a distinct contrast between the three seas–the East China Sea, the South China Sea, and the Strait of Malacca–and the Indian Ocean, with longitude 90°E serving as a dividing boundary (Fig. 5a). In terms of aerosol size, the particle size range was 50–300 nm until April 9 (i.e., at 90°E), excluding the first day of the cruise (March 28, LT), and thereafter it showed a slightly smaller range of 20–200 nm. The Aitken and accumulation modes also showed apparent differences across 90°E (Fig. 5d–e), indicating that the Indian Ocean is characterized by conditions close to those of a background atmosphere.

Meanwhile, N_{CCN} ranged from 1 to 2407 cm^{-3} at 0.2% SS and from 4 to 2670 cm^{-3} at 0.6% SS, with averages of 146 ± 232 cm^{-3} and 323 ± 348 cm^{-3}, respectively, and showed a clear contrast across 90°E (Fig. 6a–b and Fig. S4a). Although CCN covered a somewhat narrower concentration range than the total aerosols, the two concentrations exhibited remarkably similar spatiotemporal variability throughout the entire period. However, the N_{CCN}/N_{CN} ratios displayed the opposite trend, with notably higher ratios in the Indian Ocean than in other regions, particularly at higher supersaturation (Fig. 6c–d and Fig. S4b).

In the South China Sea, between 16:30 on April 1 and 02:30 on April 2 (UTC), a noticeable increase in both N_{CN} and N_{CCN} of nearly an order of magnitude was observed in the western part of Luzon Island, Philippines (near 15.5°N, 116.8°E), accompanied by high N_{CCN}/N_{CN} ratios. Notably, N_{CCN} during this period reached its maximum value for the entire cruise. A crucial point is that this period was the only instance in which the N_{CCN} at 0.2% SS, where only relatively larger aerosols can activate, were similar to those at the other supersaturations. In fact, this enhancement was primarily driven by the accumulation mode, particularly by

https://doi.org/10.5194/egusphere-2026-842
Preprint. Discussion started: 24 February 2026

particles around 200 nm in diameter, consistent with the distribution of geometric mean diameter (Fig. 5b). A detailed analysis of this phenomenon will be provided in Section 3.1.2.

Localized variation was observed within the Strait of Malacca. N_{CN} were higher upon entering the strait from the South China Sea than upon exiting into the Indian Ocean. This pattern was also evident in the spatial distributions of the three aerosol modes. When combined with the aerosol size distribution, the contrast was particularly pronounced in the Aitken mode, suggesting influence from the ship exhaust. However, the distribution of the geometric mean diameter was larger when exiting the strait. This is because the ratio of Aitken mode to accumulation mode was lower upon exiting the strait. N_{CCN} at 0.2% SS exhibited a relatively uniform distribution within the strait, whereas N_{CCN} at the other supersaturations were higher upon entering the strait, consistent with the pattern of N_{CN}. As a result, the N_{CCN}/N_{CN} ratios did not show substantial variations within the strait.

Over the Indian Ocean, on April 9 (UTC), N_{CN} and N_{CCN} decreased sharply, reaching their minimum values during the cruise. One contributing factor to this decrease was the wet deposition associated with intense precipitation. Beginning around 22:00 on April 8 (UTC), heavy rainfall occurred for about 2 hours, with a peak precipitation rate of 60 $mm\ h^{-1}$, likely scavenging a substantial fraction of atmospheric particles. Separately, a reduction in number concentrations due to intense precipitation was also observed on the first day of the cruise over the Southern Sea area of Korea.

https://doi.org/10.5194/egusphere-2026-842
Preprint. Discussion started: 24 February 2026

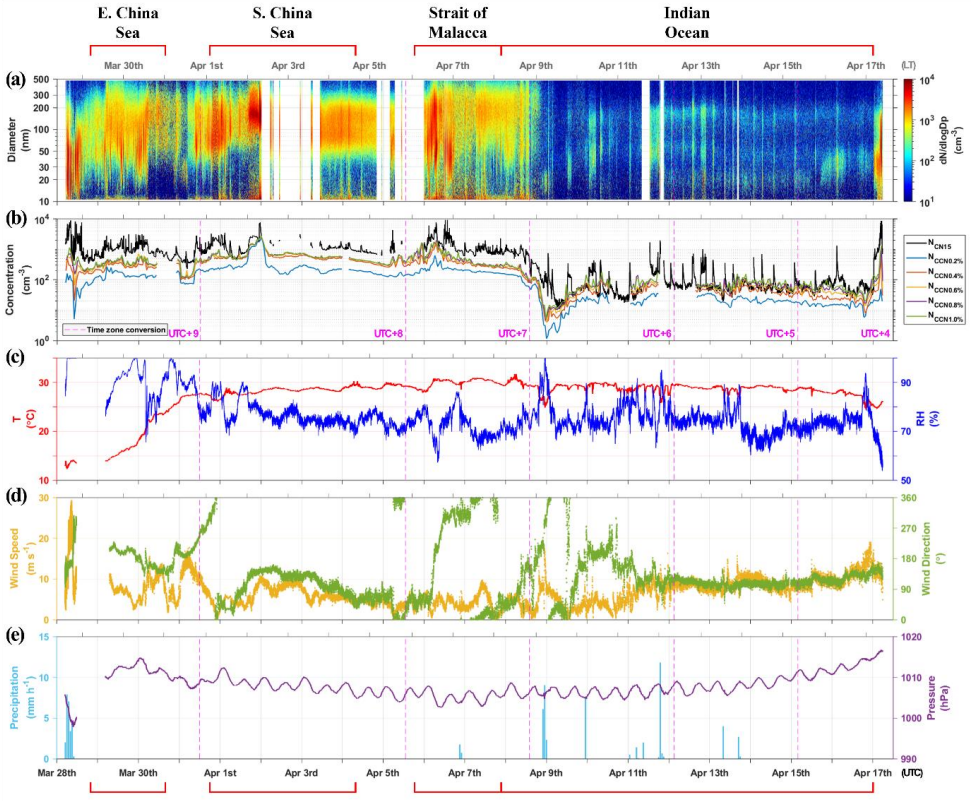

Figure 4. Time series of (a) aerosol size distribution, (b) aerosol and CCN number concentrations, (c) temperature and relative humidity (RH), (d) true wind speed and direction, and (e) precipitation and pressure during the transit voyage of the R/V *ISABU*. The top and bottom x-axis are Local Time (LT) and Coordinated Universal Time (UTC), respectively, and the x-axis tick marks indicate the midnight of each day. The vertical magenta dashed lines indicate the changes in the local time zone, with the applied time zone for each segment presented in (b).

https://doi.org/10.5194/egusphere-2026-842
Preprint. Discussion started: 24 February 2026

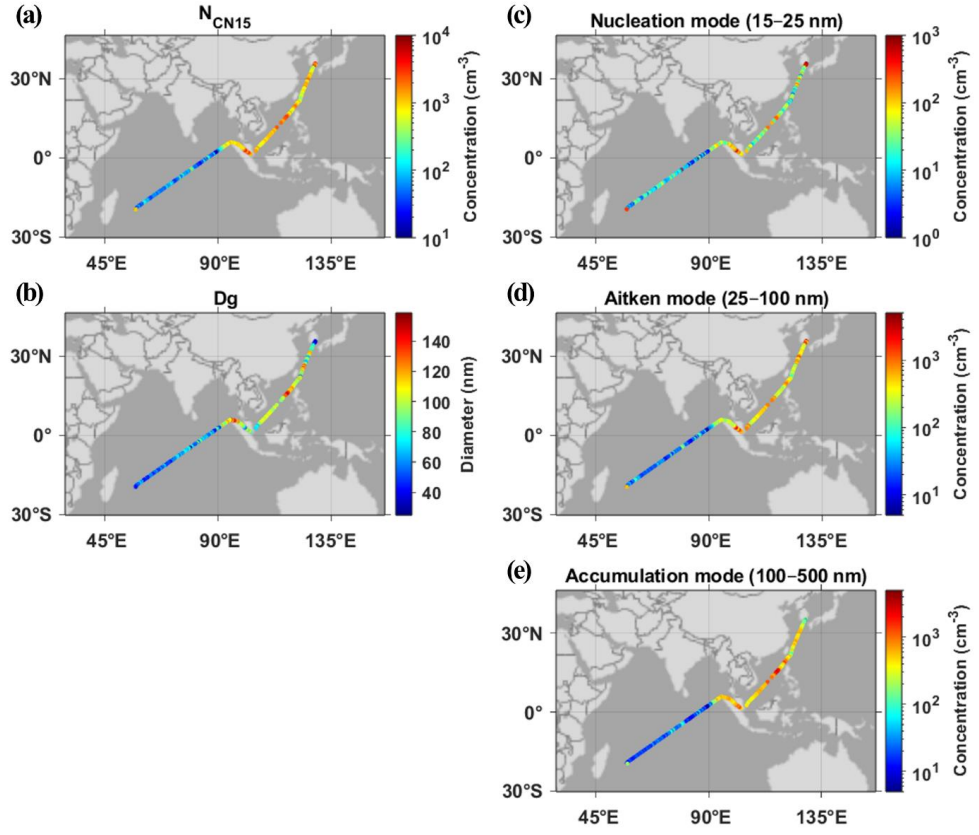

Figure 5. Spatial distributions of (a) aerosol number concentrations, (b) geometric mean diameter, and number concentrations of (c) nucleation mode (15–25 nm), (d) Aitken mode (25–100 nm), and (e) accumulation mode (100–500 nm) during the transit voyage of the R/V *ISABU* (from Natural Earth).

https://doi.org/10.5194/egusphere-2026-842
Preprint. Discussion started: 24 February 2026

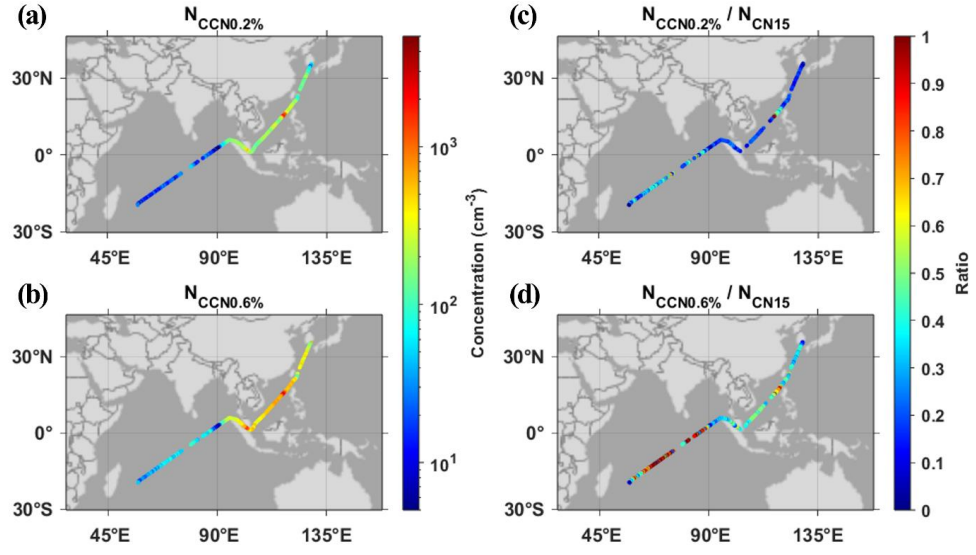

Figure 6. Spatial distributions of (a–b) CCN number concentrations at 0.2% and 0.6% supersaturation and (c–d) their ratios to aerosol number concentrations during the transit voyage of the R/V *ISABU* (from Natural Earth).

https://doi.org/10.5194/egusphere-2026-842
Preprint. Discussion started: 24 February 2026

3.1.2. Special episode: Effect of Taal Volcano

During the period from 16:30 on April 1 to 02:30 on April 2 (UTC), high N_{CN} and N_{CCN} were observed as the R/V *ISABU* passed west of Luzon Island, Philippines. Compared with the periods before and after this event, N_{CN} increased by approximately 1844 cm^{-3} (186%), and N_{CCN} at 0.2% and 0.6% SS increased by about 1167 cm^{-3} (398%) and 1037 cm^{-3} (151%), respectively.

The source of this high concentration was apparently the Taal volcano, located in the southern part of Luzon (14.010°N, 120.998°E). According to the Volcano Bulletins provided by the Philippine Institute of Volcanology and Seismology (PHIVOLCS), this active volcano exhibited intermittent eruptive activity throughout 2024. Notably, the highest SO_2 flux of 18,639 tons in 2024 was observed on March 28, just prior to the high-concentration period (Fig. S5). Another substantial flux of over 10,000 tons was recorded two days later on March 30. To assess whether emissions from the Taal volcano could have influenced the South China Sea, a back trajectory analysis was conducted. The starting altitudes for the trajectories were set to 500, 750, and 1000 m, accounting for the volcano's elevation (311 m) and the reported plume heights (900–1200 m).

Figure 7a shows the air mass back trajectories originating from three starting heights above the Taal volcano. In all cases, the trajectories passed through the region where high N_{CCN} at 0.2% SS were observed. However, if an air mass passes over a specific region above the boundary layer (BL), it may not influence the surface. Therefore, ERA5 reanalysis data were used to compare the BL height at the location of the R/V *ISABU* with the heights of the trajectories (Fig. 7b). The red dots indicate the times and heights at which each trajectory was closest to the cruise route. Many of these points lie below the BL height (indicated by the blue line) during the high-concentration period (shaded in green). This confirms that the conditions were conducive to volcanic influence reaching the near-surface marine boundary layer.

SO_2 measured by the Air Quality Monitoring System (AQMS; Thermo Fisher Scientific Inc., USA) installed on the R/V *ISABU* also showed significantly elevated concentrations in the western part of Luzon (Fig. S6), providing strong evidence that the Taal volcano was the source responsible for the high N_{CN} and N_{CCN}. Importantly, given that the observed geometric mean diameter was 141.2 ± 7.67 nm, the enhancement is unlikely to be due to primary volcanic particles such as volcanic ash, which typically have sizes of several micrometers. Instead, it

https://doi.org/10.5194/egusphere-2026-842
Preprint. Discussion started: 24 February 2026

364 was attributed to secondary aerosols formed and grown through photochemical reactions of the
365 large amounts of SO_2 emitted from the volcano (Boulon et al., 2011; Twigg et al., 2016).

366

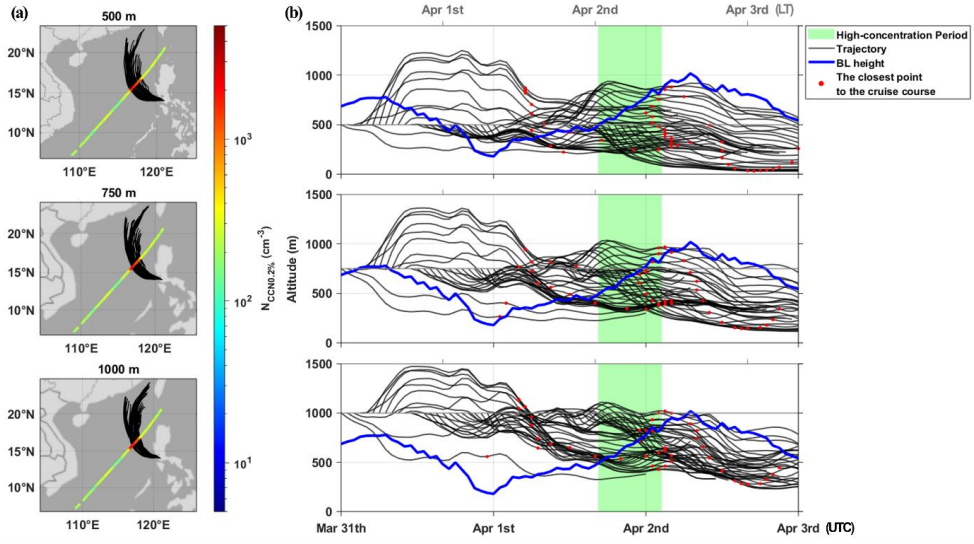

367

368 **Figure 7.** (a) A total of 48 trajectories originating at 500, 750, and 1000 m above the Taal
369 volcano at every hour from 00:00 on March 31 to 23:00 on April 1 (UTC). The color scale
370 represents CCN number concentrations at 0.2% supersaturation. Map data from Natural Earth.
371 (b) Altitudes of trajectories and boundary layer height at the location of the R/V *ISABU*. The
372 green shading indicates the volcanic-influence period from 16:30 on April 1 to 02:30 on April
373 2 (UTC). The red dots denote the times at which each trajectory was closest to the cruise route.

374

https://doi.org/10.5194/egusphere-2026-842
Preprint. Discussion started: 24 February 2026

3.2. Comparison of different sea areas

In the preceding section on spatiotemporal variations, we briefly examined the differences among the sea areas. However, because N_{CN} and N_{CCN} varied substantially across regions, we computed sea-area-specific statistics to enable quantitative comparisons of the various parameters.

3.2.1. CN and CCN number concentrations

Figure 8a shows that N_{CN} were markedly low in the Indian Ocean (150 ± 230 cm^{-3}) and increased slightly in the order of the East China Sea, the South China Sea, and the Strait of Malacca. The volcanic-influence period exhibited the highest concentration of 2834 ± 1330 cm^{-3}. The geometric mean diameter showed a pattern similar to that of N_{CN} (Fig. 8b): it was the smallest in the Indian Ocean (65.4 ± 19.9 nm) and the largest during the volcanic-influence period (141.2 ± 7.67 nm). In the Indian Ocean, all three modes exhibited the lowest number concentrations among all sea areas. During the volcanic-influence period, the Aitken mode had the second-lowest number concentration (339 ± 124 cm^{-3}, higher only than the Indian Ocean), whereas the accumulation mode showed an exceptionally high concentration (2339 ± 1127 cm^{-3}). Given that approximately 80% of the total aerosols were composed of accumulation mode particles, this finding is consistent with the geometric mean diameter results.

Meanwhile, the East China Sea, the South China Sea, and the Strait of Malacca had broadly comparable geometric mean diameters, differing by less than 10 nm. However, the number concentrations of each mode showed distinct differences among the three seas (Fig. 8c–e). The nucleation mode was the lowest in the South China Sea and the highest in the Strait of Malacca. In contrast, Aitken and accumulation modes were the lowest in the East China Sea, and although they were the highest in the Strait of Malacca, their differences relative to the South China Sea were minor.

Figure 9a–b present that N_{CCN} were the lowest in the Indian Ocean (30 ± 33 cm^{-3} at 0.2% SS and 67 ± 59 cm^{-3} at 0.6% SS) and the highest in the South China Sea during the volcanic-influence period (1460 ± 473 cm^{-3} at 0.2% SS and 1735 ± 469 cm^{-3} at 0.6% SS). However, the N_{CCN}/N_{CN} ratios were the second highest in the Indian Ocean (Fig. 9 c–d). In particular, the difference in the ratios at 0.6% SS was considerably smaller than the difference in N_{CCN} between the two regions. This suggests that, despite the smallest aerosol sizes in the Indian

https://doi.org/10.5194/egusphere-2026-842
Preprint. Discussion started: 24 February 2026

Ocean, a substantial fraction of the aerosols consisted of hygroscopic components and thus effectively acted as CCN. Meanwhile, the ratios at 0.2% SS during the volcanic-influence period were exceptionally high, reflecting not only the largest aerosol sizes but also the dominance of hygroscopic sulfate aerosols.

A notable feature emerged when comparing the South China Sea and the Strait of Malacca. Although N_{CN} were slightly higher in the Strait of Malacca (1226 ± 517 cm^{-3} in the South China Sea vs. 1446 ± 1048 cm^{-3} in the Strait of Malacca), N_{CCN} were actually slightly higher in the South China Sea (233 ± 47 cm^{-3} at 0.2% SS and 601 ± 94 cm^{-3} at 0.6% SS) than in the Strait of Malacca (224 ± 84 cm^{-3} at 0.2% SS and 536 ± 353 cm^{-3} at 0.6% SS). The N_{CCN}/N_{CN} ratios were likewise higher in the South China Sea. This suggests that aerosols in the South China Sea were more hygroscopic and therefore more readily activated as CCN than those in the Strait of Malacca. This interpretation is reasonable given the substantial ship emissions in the Strait of Malacca resulting from heavy cargo traffic.

N_{CCN} observed in this study were broadly consistent with previous studies. In the East and South China Seas, N_{CCN} has been reported to range from several hundred per cubic centimeter in remote areas (Atwood et al., 2017; Gong et al., 2023) to several thousand under continental influence (Gao et al., 2020; Ou et al., 2025). These ranges were comparable to the results of this study (Fig. 9a–b and Fig. S7a). In contrast, in the Indian Ocean, which is considered a background environment, Dournaux et al. (2025) reported N_{CCN} in the range of tens to a few hundred per cubic centimeter. These values were consistent not only with the present study but also with observations from other pristine marine regions (Park et al., 2020; Sanchez et al., 2021; Tatzelt et al., 2022).

https://doi.org/10.5194/egusphere-2026-842
Preprint. Discussion started: 24 February 2026

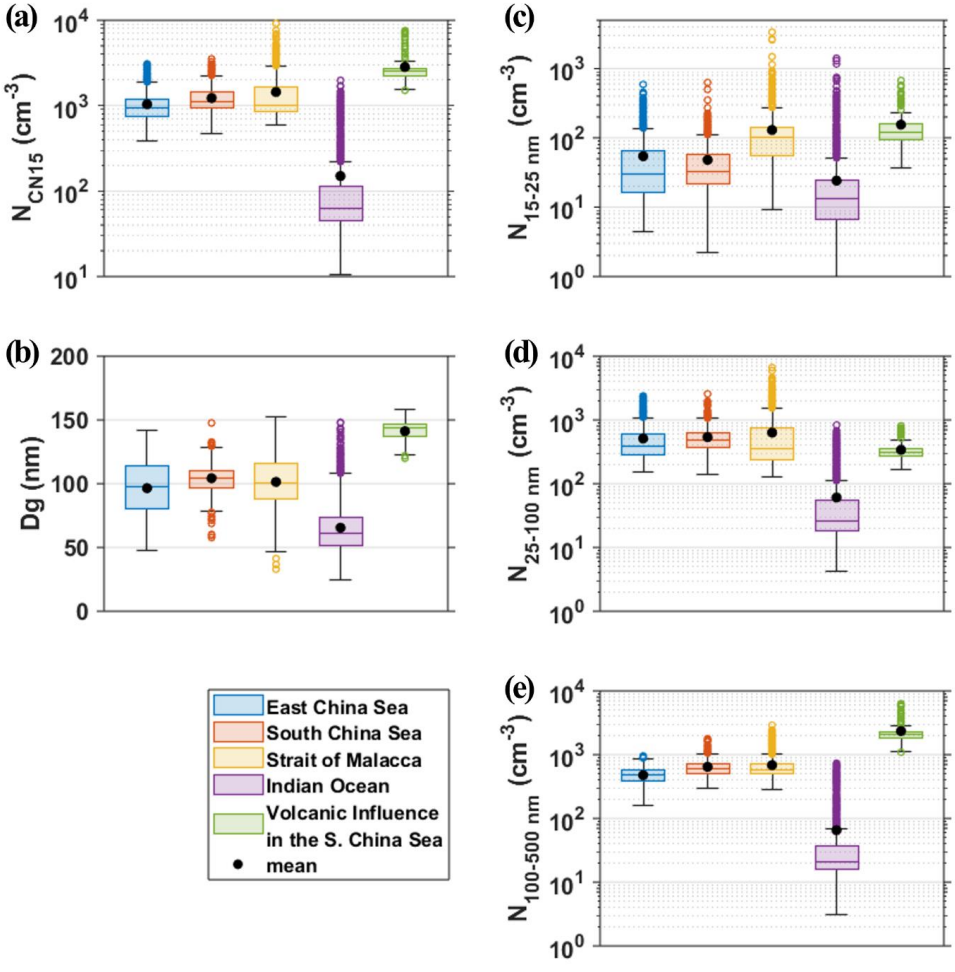

Figure 8. Box plots of (a) aerosol number concentrations, (b) geometric mean diameter, and (c) nucleation (15–25 nm), (d) Aitken (25–100 nm), and (e) accumulation (100–500 nm) mode number concentrations for each sea area. For the South China Sea, the volcanic-influence period was depicted separately. Black dots represent the mean values.

https://doi.org/10.5194/egusphere-2026-842
Preprint. Discussion started: 24 February 2026

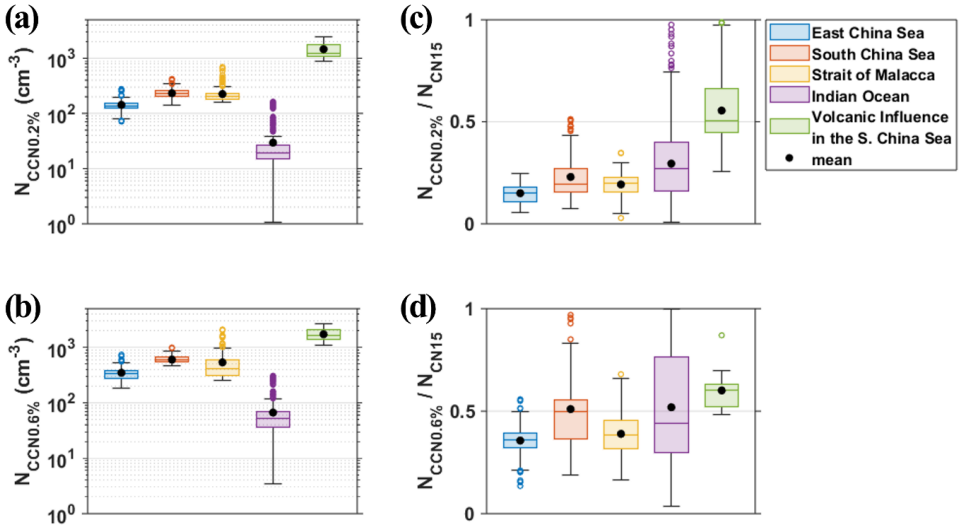

435

436 **Figure 9.** Box plots of (a–b) CCN number concentrations at 0.2% and 0.6% supersaturation
437 and (c–d) their ratios to the aerosol number concentrations for each sea area. For the South
438 China Sea, the volcanic-influence period was depicted separately. Black dots represent the
439 mean values.

440

https://doi.org/10.5194/egusphere-2026-842
Preprint. Discussion started: 24 February 2026

3.2.2. Size distributions

Figure 10 shows the average aerosol size distributions for each sea area along with the fitting results for each mode. The number of modes was empirically determined by inspecting the size distributions. The decision to include the nucleation mode was carefully made, considering occasional voltage instabilities in the smallest size bins of the SMPS.

In the East China Sea, the South China Sea, and the Strait of Malacca, two distinct modes—Aitken and accumulation—were observed. Although the relative number concentrations and contributions of these modes varied somewhat among the sea areas, these distributions appeared to reveal the typical characteristics of anthropogenic influences and secondary aerosol formation (Bates et al., 2004; Seinfeld and Pandis, 2016; Ueda et al., 2016). Notably, the Aitken mode in the Strait of Malacca showed the largest geometric standard deviation of 2.36 among all fitting results, suggesting complex mixing of marine background aerosols, continental aerosols, and ship exhaust. Consequently, given that the majority of the accumulation mode particles can act as CCN, N_{CCN} in these three regions are likely to be highly sensitive to the actual size and chemical composition of the Aitken mode, which accounts for a substantial fraction of the aerosol population.

Three distinct modes, nucleation, Aitken, and accumulation, were identified in the Indian Ocean. Among these, the accumulation mode made the most significant contribution (approximately half of the total), indicating that although N_{CN} in the Indian Ocean were significantly low, a substantial fraction of the particles could act as CCN. However, according to previous studies (Kompalli et al., 2020; Dournaux et al., 2025), even in the Indian Ocean, the dominant aerosol mode can vary by region and air mass origin, with the Aitken mode sometimes prevailing and the nucleation mode not always being observed.

Finally, during the volcanic-influence period, only a single distinct accumulation mode was observed, characterized by a very narrow distribution with a geometric standard deviation of 1.43. This is because most aerosols during this period were sulfate-dominated particles (i.e., non-sea-salt sulfate aerosols), which originated from the oxidation of SO_2 emitted by the Taal volcano and the subsequent condensation of the resulting H_2SO_4.

These results provide direct evidence that applying a single, uniform parameterization of marine aerosols in models is highly problematic and that at least regional differentiation is required to represent them. Moreover, these differences in aerosol size distributions across sea

https://doi.org/10.5194/egusphere-2026-842
Preprint. Discussion started: 24 February 2026

472 areas can lead to substantial variations in CCN efficiency for a given supersaturation condition,
473 as evaluated in terms of κ and CCN spectra in the following section.

474

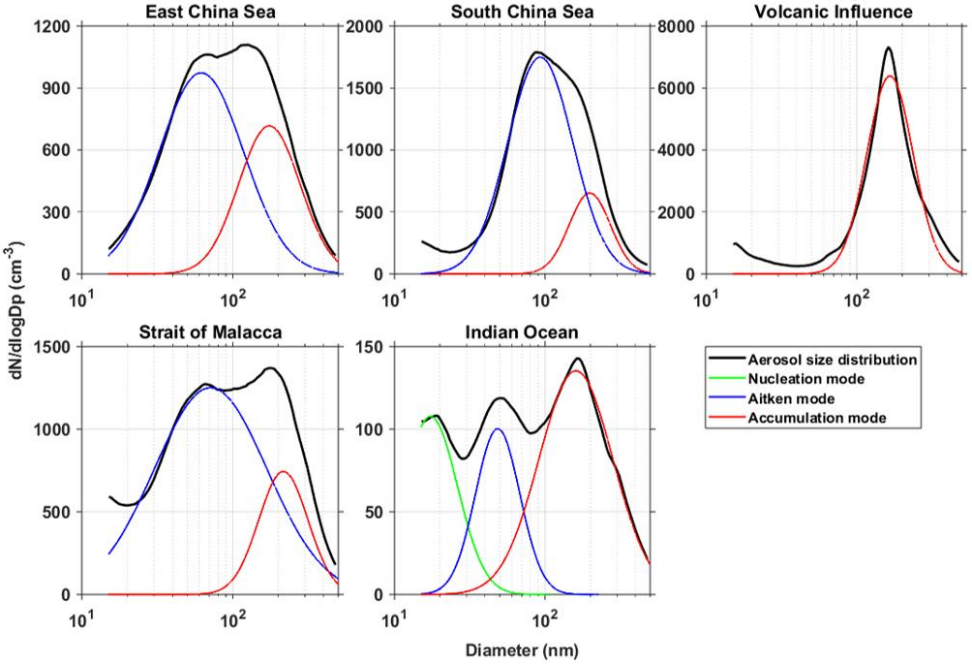

475

476 **Figure 10.** Aerosol size distributions (black) for each sea area along with the fitting results for
477 each mode (green, blue, and red). For the South China Sea, the volcanic-influence period was
478 depicted separately.

479

https://doi.org/10.5194/egusphere-2026-842
Preprint. Discussion started: 24 February 2026

3.2.3. Critical diameter and hygroscopicity

Figure 11 presents the mean and uncertainty ranges of the D_C and κ for each supersaturation for each sea area. Note that at lower supersaturations, the uncertainties in CCN measurements increase. Moreover, since SMPS measures N_{CN} in discrete size bins, D_C can fluctuate significantly with only a slight change in N_{CCN} when N_{CN} are very low. The combined effects of these factors can result in considerable uncertainties at low supersaturation (i.e., 0.2% SS), especially where N_{CN} are very low (e.g., the Indian Ocean). Therefore, our interpretation focused primarily on trends and relative comparisons.

According to Köhler theory, higher supersaturations allow progressively smaller particles to activate; consequently, the D_C for each sea area decreased with increasing supersaturation. As an exception, during the volcanic-influence period, similar D_C were observed across the 0.4–1.0% SS due to the very narrow distribution of the accumulation mode. Even at the same supersaturation, substantial differences in D_C were evident among sea areas. Larger D_C—such as those observed in the Strait of Malacca—indicate that only relatively large particles could act as CCN because they had low κ.

Interestingly, κ showed a decreasing trend with increasing supersaturation and spanned a wide range of 0.05–0.3, reflecting variations in aerosol composition and mixing state across sea areas and aerosol sizes. Higher κ values were observed in the Indian Ocean and at certain supersaturations in the South China Sea. This implies that aerosols of the same size in the two sea areas were more likely to activate as CCN at a given supersaturation compared to the other sea areas that showed lower κ values. These supersaturation-dependent D_C–κ characteristics influence aerosol activation into CCN and ultimately CCN spectra shape patterns.

The significantly low κ in the East China Sea was also reported by Gong et al. (2023). Rather than reflecting the extremely low intrinsic κ of aerosols, this was likely due to activation competition under high N_{CN} conditions with limited water vapor availability, highlighting a limitation of the CCN-derived κ method. Although the κ calculation methods differ, the κ in the South China Sea reported in previous studies (Atwood et al., 2017; Ou et al., 2025) was higher than those that obtained in this study. According to Nair et al. (2024) and Dournaux et al. (2025), κ values at 0.4% SS obtained in the Equatorial and Southern Indian Ocean were similar to those derived in this study across the Indian Ocean.

https://doi.org/10.5194/egusphere-2026-842
Preprint. Discussion started: 24 February 2026

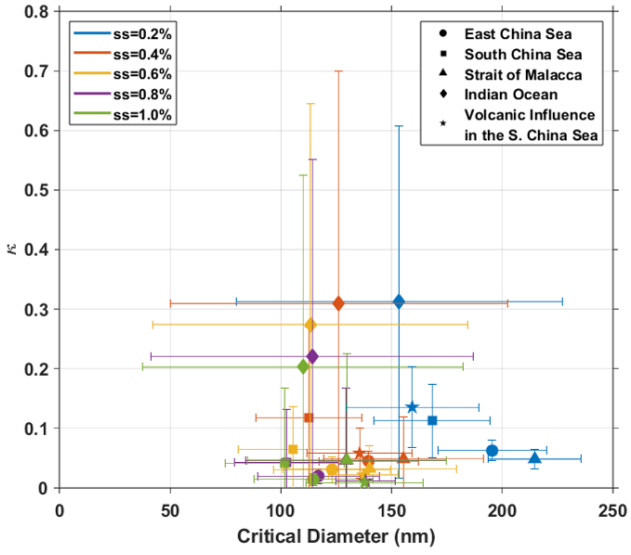

Figure 11. Distributions of the D_C and κ at given supersaturations for each sea area. The symbols represent the mean values, and the lengths of the error bars correspond to one standard deviation. For the South China Sea, the volcanic-influence period was depicted separately.

https://doi.org/10.5194/egusphere-2026-842
Preprint. Discussion started: 24 February 2026

3.2.4. CCN spectra

The measured mean CCN spectra are shown together with those fitted by a two- and three-parameter formula as shown in Figure 12. Twomey formula $N_{CCN} = C \times SS^{\alpha}$ (Twomey, 1959), where C and α are the fitting parameters, was used as the two-parameter formula. $N_{CCN} = N \times (1 - exp(-B \times SS^{\beta}))$ proposed by Ji and Shaw (1998), where N, B, and β are the fitting parameters, was used as the three-parameter formula. The parameters and coefficients of determination for the fitting are summarized in Table 1.

When applying the Twomey formula, relatively low coefficients of determination were obtained for the South China Sea and volcanic-influence period (0.783 and 0.710, respectively). In contrast, the Ji and Shaw formula yields coefficients of determination close to unity across all regions. Although this improvement was expected, given the inclusion of an additional parameter, it highlights the limitations of the traditional Twomey formula. In particular, the Twomey formula tends to overestimate N_{CCN} at low supersaturations representative of real atmospheric conditions, indicating that its application in cloud modeling requires careful consideration.

Meanwhile, as indicated by the fitted curves, the Ji and Shaw formula predicts that N_{CCN} do not increase infinitely with increasing supersaturation but instead asymptotically converge toward the parameter N closely related to N_{CN} and size distributions. Consequently, in regions with abundant CCN, such as the South China Sea and Strait of Malacca, the influence of aerosol variability on CCN is limited. In contrast, in regions with very low N_{CCN}, such as the Indian Ocean, cloud properties can change significantly as they respond sensitively to aerosol variability.

Parameter β reflects the sensitivity of N_{CCN} to supersaturation and is directly related to D_C. A larger β indicates that N_{CCN} respond more strongly to small changes in supersaturation. The effect associated with differences in β was particularly evident when comparing the South China Sea and the Strait of Malacca. Although the two sea areas exhibited similar N values, β was the highest in the South China Sea and the second lowest in the Strait of Malacca. As a result, N_{CCN} differed substantially between the two sea areas at 0.4% and 0.6% SS. This contrast could be attributed to the smaller and narrowly distributed D_C and the higher κ in the South China Sea compared to the Strait of Malacca, leading to stronger supersaturation-dependent aerosol activation. These differences in β suggest that variations in updraft velocity

https://doi.org/10.5194/egusphere-2026-842
Preprint. Discussion started: 24 February 2026

or subtle changes in thermodynamic conditions can induce substantial fluctuations in cloud microphysics.

In the case of the Indian Ocean, when compared with aircraft measurements conducted below the BL during the INDOEX campaign in 1999, the CCN spectra in this study were similar to those classified as 'Clean' in the previous work (Hudson and Yum, 2002). Considering the gap of more than 20 years between the two observation periods, this consistent result provides strong evidence that the Indian Ocean is a pristine remote ocean.

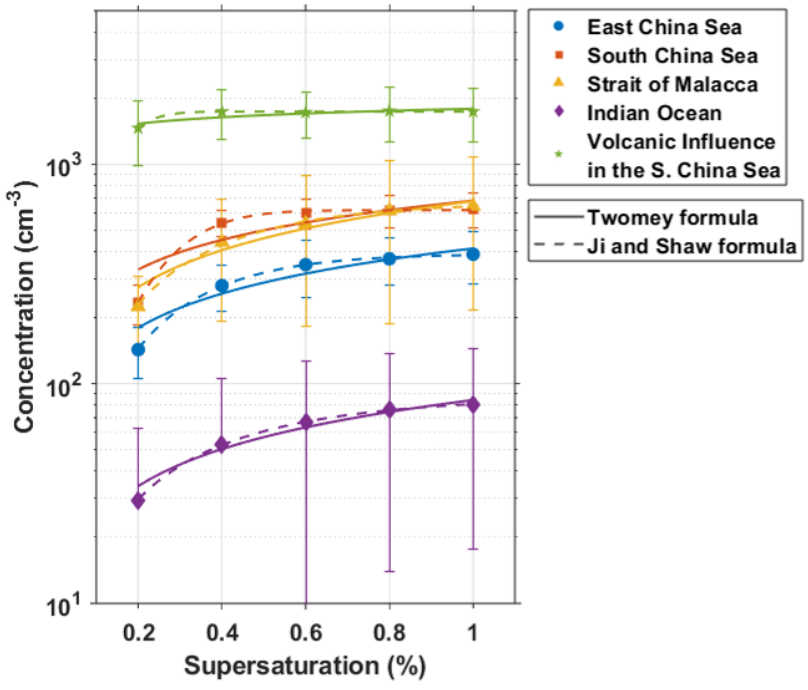

Figure 12. Fitting results of the Twomey (solid line) and Ji and Shaw (dashed line) formulas for each sea area.

https://doi.org/10.5194/egusphere-2026-842
Preprint. Discussion started: 24 February 2026

559 **Table 1**. The coefficients of determination and parameters of CCN fitting for each sea area.

	$N_{CCN} = C \times SS^{\alpha}$			$N_{CCN} = N \times (1 - exp(-B \times SS^{\beta}))$			
	R^2	C	α	R^2	N	B	β
East China Sea	0.914	413.1	0.517	0.999	388.4	4.726	1.443
South China Sea	0.783	681.6	0.449	0.998	616.6	13.77	2.089
Strait of Malacca	0.948	678.1	0.562	0.997	664.3	3.372	1.288
Indian Ocean	0.968	84.26	0.561	1.000	86.59	2.684	1.153
Volcanic influence in the S. China Sea	0.710	1787	0.097	0.995	1734	45.86	1.997

560 Note. For the South China Sea, the volcanic-influence period was depicted separately.

https://doi.org/10.5194/egusphere-2026-842
Preprint. Discussion started: 24 February 2026

3.3. Clustering analysis

Even within the same sea area, the origin of air masses could differ during the cruise, which in turn may lead to variations in the observed characteristics of aerosols and CCN. Therefore, we performed k-means clustering on the 72-hour back trajectories for the four sea areas (Fig. 13). The cluster numbers were assigned in chronological order.

The East China Sea was classified into three clusters: seas near Korea (Cluster 1), Mainland China (Cluster 2), and the Pacific Ocean (Cluster 3). In contrast to Cluster 3, which remained at relatively low altitudes, Clusters 1 and 2 were transported from altitudes exceeding 1000 m. As shown in Table 2, N_{CN} and N_{CCN} were higher when air masses originated from the continent compared to when they originated from marine regions (Note that CCN data for the Cluster 3 period are unavailable due to a CCNC instrument error). However, the N_{CCN}/N_{CN} ratios were higher in Cluster 1, which contrasts with the larger geometric mean diameter in Cluster 2. Although this study does not include aerosol chemical composition data, these results suggest that CCN activation depends not only on particle size but also strongly on chemical composition. Furthermore, it can be inferred that marine-origin aerosols are likely composed of more hygroscopic components than continental aerosols.

For the South China Sea, three clusters were identified: stagnant air masses near the Philippines and Taiwan (Cluster 1); air masses originating from the western Pacific that passed over Luzon Island (Cluster 2); and those that passed over the Visayas Islands (Cluster 3). Although all three clusters were of marine origin, the characteristics of aerosols and CCN varied significantly depending on the regions traversed by the air masses. As described in Section 3.1.2, the influence of the Taal volcano led to an exceptionally high N_{CN} of 2697 ± 1374 cm^{-3} during the Cluster 2 period. This enhancement was observed only in accumulation mode, resulting in geometric mean diameters that were 22.3 nm and 31.2 nm larger than those of Clusters 1 and 3, respectively. Moreover, the substantial fraction of larger sulfate aerosols in Cluster 2 led to N_{CCN} during this period being at least twice that observed in Clusters 1 and 3, with the difference being particularly evident at 0.2% SS. Meanwhile, Clusters 1 and 3 exhibited similar number concentrations of nucleation and Aitken modes, whereas those of the accumulation mode were approximately 100 cm^{-3} higher during the Cluster 1 period. Consequently, the geometric mean diameter in Cluster 1 was slightly larger than that in Cluster 3, and N_{CCN} at 0.2% SS were also higher during the Cluster 1 period. At other supersaturations,

https://doi.org/10.5194/egusphere-2026-842
Preprint. Discussion started: 24 February 2026

N_{CCN} were comparable between Cluster 1 and 3, although the N_{CCN}/N_{CN} ratios were somewhat higher in Cluster 1.

The Strait of Malacca was divided into two clusters, both of marine origin, but associated with different source regions: the South China Sea (Cluster 1) and the Andaman Sea (Cluster 2). Notably, unlike Cluster 2, which remained exclusively over the marine region, Cluster 1 traversed Peninsular Malaysia at low altitudes, indicating a potential terrestrial influence. As a result, not only N_{CN} but also the number concentrations of each mode were approximately twice as high in Cluster 1. Although the geometric mean diameter was slightly larger in Cluster 2, the substantially higher N_{CN} in Cluster 1 led to much higher N_{CCN} across all supersaturations during the Cluster 1 period. The N_{CCN}/N_{CN} ratios, however, were higher during the Cluster 2 period at 0.2% SS, while at the remaining four supersaturations, they were higher during the Cluster 1 period.

In the Indian Ocean, the air masses were categorized into three origins: the Bay of Bengal (Cluster 1), the southeastern Indian Ocean (Cluster 2), and the southwestern Indian Ocean (Cluster 3). As in the South China Sea, all clusters were of marine origin; however, unlike the South China Sea, extended back trajectories indicate that their origins may trace back to land (Fig. S8). Despite the occurrence of the lowest N_{CN} due to intense precipitation during the Cluster 1 period, N_{CN} and N_{CCN} were the highest among the three clusters. This is likely because the Bay of Bengal is adjacent to land, allowing continental aerosols to be transported under northerly winds. Consequently, the N_{CCN}/N_{CN} ratios were lower than those of the two clusters originating from the Indian Ocean. Comparing the two Indian Ocean clusters, higher N_{CN} and N_{CCN} were observed in Cluster 2, which was influenced by southeasterly winds, with the difference particularly pronounced at 0.4% SS. Back trajectories extended to 120 hours further suggest that the Australian continent may have influenced the elevated number concentrations during the Cluster 2 period.

https://doi.org/10.5194/egusphere-2026-842
Preprint. Discussion started: 24 February 2026

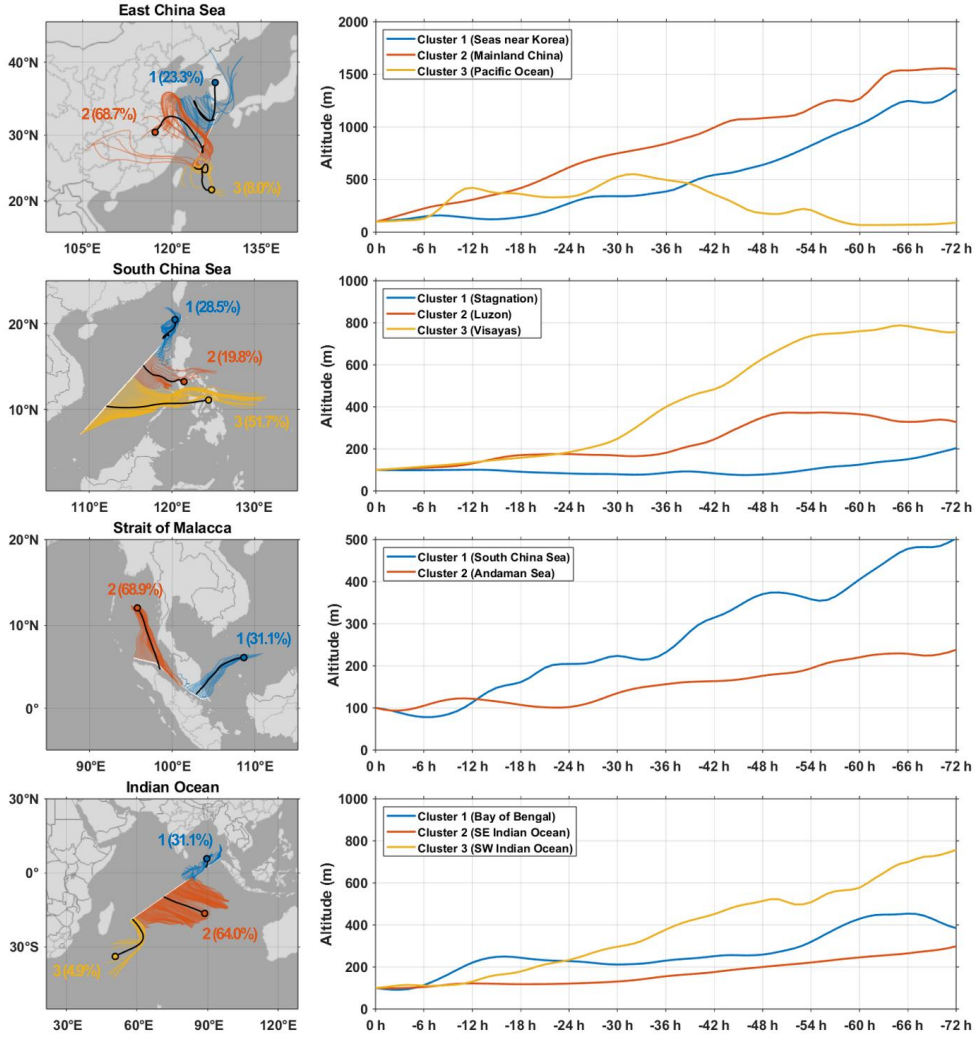

Figure 13. Cluster analysis results for each sea area and mean altitude variations of 72 hours back trajectories within each cluster. The thick black solid lines with dots at their ends represent the mean trajectories of each cluster. The percentages in parentheses indicate the proportion of trajectories assigned to each cluster. Map data from Natural Earth.

https://doi.org/10.5194/egusphere-2026-842
Preprint. Discussion started: 24 February 2026

Table 2. Aerosol number concentrations and geometric mean diameter, CCN number concentrations, and the CCN-to-aerosol ratio for each cluster in each sea area.

	East China Sea			South China Sea			Strait of Malacca		Indian Ocean		
	Seas near Korea	Mainland China	Pacific	Stagnation	Luzon	Visayas	South China Sea	Andaman Sea	Bay of Bengal	SE Indian Ocean	SW Indian Ocean
Aerosols (cm^{-3})											
Total	774 ± 346	1162 ± 453	755 ± 118	1299 ± 690	2697 ± 1374	1171 ± 281	2311 ± 1240	1192 ± 828	281 ± 335	90 ± 115	55 ± 17
Nucleation	58 ± 60	56 ± 67	19 ± 12	52 ± 51	148 ± 118	45 ± 39	183 ± 322	115 ± 143	28 ± 34	23 ± 63	8 ± 4
Aitken	397 ± 225	576 ± 379	280 ± 45	527 ± 382	429 ± 222	516 ± 116	1093 ± 744	495 ± 620	108 ± 130	39 ± 48	30 ± 12
Accumulation	319 ± 156	531 ± 105	462 ± 93	721 ± 381	2120 ± 1264	610 ± 143	1035 ± 502	581 ± 158	145 ± 192	28 ± 22	16 ± 4
Dg (nm)	83.1 ± 13.7	98.5 ± 21.0	117.1 ± 8.1	109.8 ± 15.1	132.1 ± 20.1	100.9 ± 5.9	90.9 ± 17.5	104.4 ± 22.6	77.9 ± 25.6	59.7 ± 12.9	56.6 ± 9.5
CCN (cm^{-3})											
0.2% SS	122 ± 48	150 ± 30	–	303 ± 172	902 ± 735	214 ± 43	283 ± 128	197 ± 24	48 ± 52	21 ± 6.3	13 ± 4
0.4% SS	217 ± 64	302 ± 53	–	570 ± 207	1187 ± 680	533 ± 62	669 ± 318	334 ± 91	80 ± 80	40 ± 14	19 ± 6
0.6% SS	285 ± 76	371 ± 100	–	630 ± 251	1255 ± 630	601 ± 84	882 ± 450	378 ± 105	95 ± 90	54 ± 17	27 ± 9
0.8% SS	310 ± 63	392 ± 86	–	636 ± 211	1273 ± 663	613 ± 89	1038 ± 493	413 ± 162	99 ± 94	65 ± 21	38 ± 22
1.0% SS	323 ± 81	410 ± 100	–	624 ± 185	1275 ± 644	625 ± 93	1120 ± 441	434 ± 185	103 ± 94	71 ± 25	37 ± 10

https://doi.org/10.5194/egusphere-2026-842
Preprint. Discussion started: 24 February 2026

625

Ratio												
0.2% SS	0.17 ± 0.06	0.14 ± 0.04	–	0.29 ± 0.15	0.47 ± 0.26	0.18 ± 0.03	0.16 ± 0.06	0.20 ± 0.06	0.24 ± 0.18	0.33 ± 0.17	0.27 ± 0.12
0.4% SS	0.32 ± 0.07	0.28 ± 0.07	–	0.56 ± 0.24	0.52 ± 0.15	0.43 ± 0.05	0.39 ± 0.13	0.33 ± 0.10	0.33 ± 0.21	0.56 ± 0.24	0.37 ± 0.19
0.6% SS	0.40 ± 0.09	0.34 ± 0.07	–	0.56 ± 0.22	0.55 ± 0.13	0.47 ± 0.07	0.46 ± 0.12	0.37 ± 0.10	0.40 ± 0.24	0.62 ± 0.26	0.51 ± 0.20
0.8% SS	0.40 ± 0.11	0.36 ± 0.07	–	0.56 ± 0.21	0.54 ± 0.12	0.48 ± 0.07	0.52 ± 0.17	0.40 ± 0.12	0.40 ± 0.25	0.60 ± 0.25	0.61 ± 0.21
1.0% SS	0.44 ± 0.08	0.39 ± 0.06	–	0.56 ± 0.23	0.56 ± 0.16	0.48 ± 0.08	0.50 ± 0.15	0.42 ± 0.14	0.38 ± 0.23	0.65 ± 0.23	0.66 ± 0.23

https://doi.org/10.5194/egusphere-2026-842
Preprint. Discussion started: 24 February 2026

4. Conclusions

This study presents a comprehensive analysis of marine aerosols and cloud condensation nuclei (CCN) characteristics across the East China Sea, the South China Sea, the Strait of Malacca, and the Indian Ocean, based on continuous measurements conducted during a long-distance transit voyage of the R/V *ISABU* operated by KIOST in 2024. The primary objective of this study was to address the limitations of previous marine observations, which were confined to a single sea area or short-term campaigns, and to robustly intercompare the characteristics of aerosols and CCN across various sea areas under a consistent observational and analytical framework. Furthermore, clustering analysis was combined to enable a multifaceted examination of variability within individual sea areas.

Throughout the entire observation period, aerosol (CN) and CCN number concentrations (N_{CN} and N_{CCN}) exhibited significant spatiotemporal variability, ranging from tens (or even a single digit) to several thousand per cubic centimeter. The lowest N_{CN} and N_{CCN} occurred locally on April 9 due to intense precipitation, a meteorological factor. In contrast, the highest N_{CCN} were observed regionally on April 2 while the vessel was cruising the western part of Luzon Island, Philippines. This high-concentration episode was driven by the Taal volcano located in the southern part of Luzon Island, and it was the only period during which N_{CCN} at 0.2% supersaturation (SS) were close to those at higher supersaturations.

Spatially, a distinct contrast in N_{CN} and N_{CCN} was observed across 90°E between continent-adjacent seas—the East China Sea, the South China Sea, and the Strait of Malacca—and the remote Indian Ocean. A similar contrast was observed in the CCN-to-aerosol (N_{CCN}/N_{CN}) ratios across the same longitude; however, the higher values were observed in the Indian Ocean. Together, these findings indicate that the Indian Ocean represents a clean background region distinct from other sea areas, characterized by low N_{CN} but composed of hygroscopic particles.

A quantitative comparison of characteristics for each sea area shows that the East China Sea, the South China Sea, and the Strait of Malacca exhibited similar N_{CN} and geometric mean diameters. These three regions were characterized by bimodal distributions with Aitken and accumulation modes, although their relative contributions varied slightly. However, N_{CCN} were higher in the South China Sea than in the Strait of Malacca. This indicates that aerosols in the South China Sea were more hygroscopic and thus more readily activated into CCN than those in the Strait of Malacca, a conclusion supported by the critical diameter and κ analyses.

https://doi.org/10.5194/egusphere-2026-842
Preprint. Discussion started: 24 February 2026

Compared with other regions, the Indian Ocean exhibited N_{CN} and N_{CCN} that were nearly an order of magnitude lower. It was also the only region characterized by a distinct nucleation mode, resulting in the smallest geometric mean diameters among all regions. Nevertheless, the Indian Ocean showed the highest κ values, indicating that the aerosols were highly hygroscopic and that a substantial fraction of the particles could act as CCN at the given supersaturations.

During the volcanic-influence period, N_{CN} and N_{CCN}, the N_{CCN}/N_{CN} ratios, and the geometric mean diameter were all at their highest levels. Since the majority of particles were in the accumulation mode and dominated by natural sulfate aerosols, N_{CCN} and their ratios were particularly elevated at 0.2% SS. Taken together, these results demonstrate that CCN activation in the marine environment is not solely governed by supersaturation but also by the combined effects of number concentration, size distribution, and κ.

In the CCN spectra, the classical Twomey formula failed to adequately capture the nonlinear increase in N_{CCN} in some regions. In contrast, the Ji and Shaw formula demonstrated excellent agreement across all regions, including the volcanic-influence period. The parameter N, representing the upper limit of N_{CCN}, was the smallest in the Indian Ocean, suggesting that cloud properties in the Indian Ocean can be susceptible to variations in aerosols. Although the South China Sea and the Strait of Malacca exhibited similar N values, the β, reflecting the sensitivity of N_{CCN} to supersaturation, was substantially larger in the South China Sea, consistent with the smaller critical diameters and more hygroscopic aerosols observed in that region.

The clustering analysis showed that in both the East China Sea and Indian Ocean, N_{CN} and N_{CCN} were higher when air masses originated from land than from the ocean. In contrast, the N_{CCN}/N_{CN} ratios were higher for marine-origin air masses, indicating that marine aerosols are more hygroscopic than continental aerosols. In the South China Sea and the Strait of Malacca, the results further demonstrate that, even for marine-origin air masses, the characteristics of aerosols and CCN can vary significantly depending on the regions traversed during transport. These findings suggest that it is essential to simultaneously consider the origins and transport pathways of air masses beyond the simple geographical classification of polluted and background areas.

The results of this study demonstrate that a single, uniform marine regime cannot represent the characteristics of marine aerosols and CCN; instead, they exhibit structurally distinct characteristics depending on the sea area and air mass origin. These measurement-based

https://doi.org/10.5194/egusphere-2026-842
Preprint. Discussion started: 24 February 2026

findings are expected to provide important constraints on improving climate and cloud models for simulating aerosol–cloud interactions in marine low-level clouds more realistically.

Nevertheless, this study was unable to resolve seasonal differences, nor did it include integrated analyses with other observational datasets (e.g., aerosol chemical composition, VOCs, or ice-nucleating particles). Therefore, future research should include comprehensive analyses integrating long-term, repeated measurements across multiple sea areas to better characterize the seasonal and interannual variability of aerosols and CCN. In addition, concurrent cloud microphysical observations are required to further elucidate aerosol–cloud interactions in greater depth.

https://doi.org/10.5194/egusphere-2026-842
Preprint. Discussion started: 24 February 2026

Code and data availability

The code and data used for figures and tables are available via https://doi.org/10.6084/m9.figshare.31315192 (Ahn et al., 2026). The SO_2 flux and plume height data for the Taal Volcano used in Section 3.1.2 were obtained from the Volcano Bulletin of the Philippine Institute of Volcanology and Seismology (PHIVOLCS) and are available via https://wovodat.phivolcs.dost.gov.ph/bulletin/list-of-bulletin. The back trajectory and height data for the air masses used in Section 3.1.2 and 3.3 were obtained using Version 5.1 of the HYSPLIT model from NOAA Air Resources Laboratory, and HYSPLIT model is available via https://www.ready.noaa.gov/documents/Tutorial/html/install_win.html. The BL height used in Section 3.1.2 were obtained from the ERA5 reanalysis data of the European Centre for Medium-Range Weather Forecasts and are available via https://cds.climate.copernicus.eu/cdsapp#!/dataset/reanalysis-era5-single-levels?tab=form (Hersbach et al., 2020).

Author contribution

CA conceptualized the overall study. CA, AL, NK, JGA, KHK, DK, and DHP carried out the installation and calibration of instruments. CA, AL, and JGA performed measurements for cloud condensation nuclei, aerosol size distribution, and sulfur dioxide, respectively, during the cruise. CA, AL, and JGA processed and validated the observational datasets. CA developed methodology, performed formal analysis, and visualized the results. UHY and SC acquired the funding, and UHY was responsible for project administration. CA wrote the paper, and NK and SSY reviewed the paper with contributions from all co-authors. AL, NK and SSY provided useful comments on the analysis.

Competing interests

The authors declare that they have no known competing financial interests or personal relationships that could have appeared to influence the work reported in this paper.

Acknowledgments

https://doi.org/10.5194/egusphere-2026-842
Preprint. Discussion started: 24 February 2026

We are deeply grateful to the Korea Institute of Ocean Science and Technology for the support provided by the R/V *ISABU* and its crew, and their help in the installation of instruments. Further, we acknowledge the Philippine Institute of Volcanology and Seismology (PHIVOLCS), the NOAA Air Resources Laboratory (ARL), and the European Centre for Medium-Range Weather Forecasts (ECMWF) for providing Volcano Bulletins, HYSPLIT model, ERA5 reanalysis, respectively, used in this study.

Financial support

This work was supported by the grant "Development of Weather Modification Technology for Climate Change" from the Korea Institute of Science and Technology (26E0111), the grant "Establishing a Research Platform for Marine Aerosol Studies Leveraging Research Vessel Transit Voyages" from the Korea Institute of Ocean Science and Technology (PEA0272), and the Yonsei Signature Research Cluster Program of 2025-22-0242.

References

Ahn, C., Loh, A., Kim, N., Yim, U. H., An, J. G., Kim, K. H., Kim, D., Park, D.-H., Yum, S. S., and Choi, S.: Characteristics of marine aerosols and cloud condensation nuclei measured during the cruise of R/V ISABU in 2024: from the East China Sea to the Indian Ocean, figshare [data set], https://doi.org/10.6084/m9.figshare.31315192, 2026.

Albrecht, B. A.: Aerosols, Cloud Microphysics and Fractional Cloudiness, Science, 245, 1227–1230, https://doi.org/10.1126/science.245.4923.1227, 1989.

Andreae, M. O. and Crutzen, P. J.: Atmospheric Aerosols: Biogeochemical Sources and Role in Atmospheric Chemistry, Science, 276, 1052–1058, https://doi.org/10.1126/science.276.5315.1052, 1997.

Aswini, M. A., Tiwari, S., Singh, U., Kurian, S., Patel, A., Gunthe, S. S., and Kumar, A.: Aeolian Dust and Sea Salt in Marine Aerosols over the Arabian Sea during the Southwest Monsoon: Sources and Spatial Variability, ACS Earth Space Chem., 6, 1044–1058, https://doi.org/10.1021/acsearthspacechem.1c00400, 2022.

Atwood, S. A., Reid, J. S., Kreidenweis, S. M., Black, D. R., Jonsson, H. H., Lagrosas, N. D., Xian, P., Reid, E. A., Sessions, W. R., and Simpas, J. B.: Size-resolved aerosol and cloud

https://doi.org/10.5194/egusphere-2026-842
Preprint. Discussion started: 24 February 2026

condensation nuclei (CCN) properties in the remote marine South China Sea – Part 1: Observations and source classification, Atmos. Chem. Phys., 17, 1105–1123, https://doi.org/10.5194/acp-17-1105-2017, 2017.

Bates, T. S., Quinn, P. K., Coffman, D. J., Covert, D. S., Miller, T. L., Johnson, J. E., Carmichael, G. R., Uno, I., Guazzotti, S. A., Sodeman, D. A., Prather, K. A., Rivera, M., Russell, L. M., and Merrill, J. T.: Marine boundary layer dust and pollutant transport associated with the passage of a frontal system over eastern Asia, J. Geophys. Res.-Atmos., 109, D19S19, https://doi.org/10.1029/2003JD004094, 2004.

Bellouin, N., Quaas, J., Gryspeerdt, E., Kinne, S., Stier, P., Watson-Parris, D., Boucher, O., Carslaw, K. S., Christensen, M., Daniau, A.-L., Dufresne, J.-L., Feingold, G., Fiedler, S., Forster, P., Gettelman, A., Haywood, J. M., Lohmann, U., Malavelle, F., Mauritsen, T., McCoy, D. T., Myhre, G., Mülmenstädt, J., Neubauer, D., Possner, A., Rugenstein, M., Sato, Y., Schulz, M., Schwartz, S. E., Sourdeval, O., Storelvmo, T., Toll, V., Winker, D., and Stevens, B.: Bounding Global Aerosol Radiative Forcing of Climate Change, Rev. Geophys., 58, e2019RG000660, https://doi.org/10.1029/2019RG000660, 2020.

Boulon, J., Sellegri, K., Hervo, M., and Laj, P.: Observations of nucleation of new particles in a volcanic plume, Proc. Natl. Acad. Sci. USA, 108, 12223–12226, https://doi.org/10.1073/pnas.1104923108, 2011.

Carslaw, K. S., Lee, L. A., Reddington, C. L., Pringle, K. J., Rap, A., Forster, P. M., Mann, G. W., Spracklen, D. V., Woodhouse, M. T., Regayre, L. A., and Pierce, J. R.: Large contribution of natural aerosols to uncertainty in indirect forcing, Nature, 503, 67–71, https://doi.org/10.1038/nature12674, 2013.

Chen, Y., Haywood, J., Wang, Y., Malavelle, F., Jordan, G., Peace, A., Partridge, D. G., Cho, N., Oreopoulos, L., Grosvenor, D., Field, P., Allan, R. P., and Lohmann, U.: Substantial cooling effect from aerosol-induced increase in tropical marine cloud cover, Nat. Geosci., 17, 404–410, https://doi.org/10.1038/s41561-024-01427-z, 2024.

Coggon, M. M., Sorooshian, A., Wang, Z., Craven, J. S., Metcalf, A. R., Lin, J. J., Nenes, A., Jonsson, H. H., Flagan, R. C., and Seinfeld, J. H.: Observations of continental biogenic impacts on marine aerosol and clouds off the coast of California, J. Geophys. Res.-Atmos., 119, 6724–6748, https://doi.org/10.1002/2013JD021228, 2014.

https://doi.org/10.5194/egusphere-2026-842
Preprint. Discussion started: 24 February 2026

788 Dournaux, M., Tulet, P., Pianezze, J., Brioude, J., Metzger, J.-M., Thyssen, M., and Athier,
789 G.: Origin, size distribution, and hygroscopic properties of marine aerosols in the
790 southwestern Indian Ocean: results of six campaigns of shipborne observations, Atmos.
791 Chem. Phys., 25, 10315–10335, https://doi.org/10.5194/acp-25-10315-2025, 2025.

792 Fan, J., Wang, Y., Rosenfeld, D., and Liu, X.: Review of Aerosol–Cloud Interactions:
793 Mechanisms, Significance, and Challenges, J. Atmos. Sci., 73, 4221–4252,
794 https://doi.org/10.1175/JAS-D-16-0037.1, 2016.

795 Flores, J. M., Bourdin, G., Altaratz, O., Trainic, M., Lang-Yona, N., Dzimban, E., Steinau, S.,
796 Tettich, F., Planes, S., Allemand, D., Agostini, S., Banaigs, B., Boissin, E., Boss, E.,
797 Douville, E., Forcioli, D., Furla, P., Galand, P. E., Sullivan, M. B., Gilson, É., Lombard,
798 F., Moulin, C., Pesant, S., Poulain, J., Reynaud, S., Romac, S., Sunagawa, S., Thomas, O.
799 P., Troublé, R., de Vargas, C., Vega Thurber, R., Voolstra, C. R., Wincker, P., Zoccola,
800 D., Bowler, C., Gorsky, G., Rudich, Y., Vardi, A., and Koren, I.: *Tara* Pacific
801 Expedition's Atmospheric Measurements of Marine Aerosols across the Atlantic and
802 Pacific Oceans, B. Am. Meteorol. Soc., 101, E536–E554, https://doi.org/10.1175/BAMS-
803 D-18-0224.1, 2020.

804 Forster, P., Storelvmo, T., Armour, K., Collins, W., Dufresne, J.-L., Frame, D., Lunt, D. J.,
805 Mauritsen, T., Palmer, M. D., Watanabe, M., Wild, M., and Zhang, H.: The Earth's
806 Energy Budget, Climate Feedbacks, and Climate Sensitivity, in: Climate Change 2021:
807 The Physical Science Basis, Contribution of Working Group I to the Sixth Assessment
808 Report of the Intergovernmental Panel on Climate Change, edited by: Masson-Delmotte,
809 V., Zhai, P., Pirani, A., et al., Cambridge University Press, Cambridge, UK and New
810 York, NY, USA, 923–1054, https://doi.org/10.1017/9781009157896.009, 2021.

811 Gao, Y., Zhang, D., Wang, J., Gao, H., and Yao, X.: Variations in N_{CN} and N_{CCN} over
812 marginal seas in China related to marine traffic emissions, new particle formation and
813 aerosol aging, Atmos. Chem. Phys., 20, 9665–9677, https://doi.org/10.5194/acp-20-9665-
814 2020, 2020.

815 Gaston, C. J., Cahill, J. F., Collins, D. B., Suski, K. J., Ge, J. Y., Barkley, A. E., and Prather,
816 K. A.: The Cloud Nucleating Properties and Mixing State of Marine Aerosols Sampled
817 along the Southern California Coast, Atmosphere, 9, 52,
818 https://doi.org/10.3390/atmos9020052, 2018.

https://doi.org/10.5194/egusphere-2026-842
Preprint. Discussion started: 24 February 2026

819 Gong, J., Zhu, Y., Chen, D., Gao, H., Shen, Y., Gao, Y., and Yao, X.: The occurrence of
820 lower-than-expected bulk N_{CCN} values over the marginal seas of China – Implications for
821 competitive activation of marine aerosols, Sci. Total Environ., 858, 159938,
822 https://doi.org/10.1016/j.scitotenv.2022.159938, 2023.

823 Haywood, J. and Boucher, O.: Estimates of the direct and indirect radiative forcing due to
824 tropospheric aerosols: A review, Rev. Geophys., 38, 513–543,
825 https://doi.org/10.1029/1999RG000078, 2000.

826 Hersbach, H., Bell, B., Berrisford, P., Hirahara, S., Horányi, A., Muñoz-Sabater, J., Nicolas,
827 J., Peubey, C., Radu, R., Schepers, D., Simmons, A., Soci, C., Abdalla, S., Abellan, X.,
828 Balsamo, G., Bechtold, P., Biavati, G., Bidlot, J., Bonavita, M., De Chiara, G., Dahlgren,
829 P., Dee, D., Diamantakis, M., Dragani, R., Flemming, J., Forbes, R., Fuentes, M., Geer,
830 A., Haimberger, L., Healy, S., Hogan, R. J., Hólm, E., Janisková, M., Keeley, S.,
831 Laloyaux, P., Lopez, P., Lupu, C., Radnoti, G., de Rosnay, P., Rozum, I., Vamborg, F.,
832 Villaume, S., and Thépaut, J. N.: The ERA5 global reanalysis, Q. J. Roy. Meteorol. Soc.,
833 146, 1999–2049, https://doi.org/10.1002/qj.3803, 2020.

834 Hudson, J. G. and Yum, S. S.: Cloud condensation nuclei spectra and polluted and clean
835 clouds over the Indian Ocean, J. Geophys. Res.-Atmos., 107, 8022,
836 https://doi.org/10.1029/2001JD000829, 2002.

837 Ji, Q. and Shaw, G. E.: On supersaturation spectrum and size distributions of cloud
838 condensation nuclei, Geophys. Res. Lett., 25, 1903–1906,
839 https://doi.org/10.1029/98GL01404, 1998.

840 King, S. M., Butcher, A. C., Rosenoern, T., Coz, E., Lieke, K. I., de Leeuw, G., Nilsson, E.
841 D., and Bilde, M.: Investigating Primary Marine Aerosol Properties: CCN Activity of Sea
842 Salt and Mixed Inorganic-Organic Particles, Environ. Sci. Technol., 46, 10405–10412,
843 https://doi.org/10.1021/es300574u, 2012.

844 Kompalli, S. K., Nair, V. S., Jayachandran, V., Gogoi, M. M., and Babu, S. S.: Particle
845 number size distributions and new particle formation events over the northern Indian
846 Ocean during continental outflow, Atmos. Environ., 238, 117719,
847 https://doi.org/10.1016/j.atmosenv.2020.117719, 2020.

https://doi.org/10.5194/egusphere-2026-842
Preprint. Discussion started: 24 February 2026

Kumar, H. and Tiwari, S.: Radiative forcing due to aerosol-cloud interactions for shallow warm clouds over the Northern Indian Ocean, Atmos. Res., 327, 108368, https://doi.org/10.1016/j.atmosres.2025.108368, 2026.

Lewis, E. R. and Schwartz, S. E.: Sea salt aerosol production: mechanisms, methods, measurements and models – a critical review, Geophys. Monogr. Ser., 152, 413 pp., American Geophysical Union, Washington, D.C., https://doi.org/10.1029/GM152, 2004.

Martin, M., Chang, R. Y.-W., Sierau, B., Sjogren, S., Swietlicki, E., Abbatt, J. P. D., Leck, C., and Lohmann, U.: Cloud condensation nuclei closure study on summer arctic aerosol, Atmos. Chem. Phys., 11, 11335–11350, https://doi.org/10.5194/acp-11-11335-2011, 2011.

Miller, R. M., Rauber, R. M., Di Girolamo, L., Rilloraza, M., Fu, D., McFarquhar, G. M., Nesbitt, S. W., Ziemba, L. D., Woods, S., and Thornhill, K. L.: Influence of natural and anthropogenic aerosols on cloud base droplet size distributions in clouds over the South China Sea and West Pacific, Atmos. Chem. Phys., 23, 8959–8977, https://doi.org/10.5194/acp-23-8959-2023, 2023.

Monahan, E. C., Spiel, D. E., and Davidson, K. L.: A model of Marine Aerosol Generation Via Whitecaps and Wave Disruption, in: Oceanic Whitecaps: And Their Role in Air-Sea Exchange Processes, edited by: Monahan, E. C. and Niocaill, G. M., Springer Netherlands, Dordrecht, 167–174, ISBN 978-94-009-4668-2, https://doi.org/10.1007/978-94-009-4668-2_16, 1986.

Moorthy, K. K. and Babu, S. S.: Aerosol Characteristics and Radiative Impacts over the Arabian Sea during the Intermonsoon Season: Results from ARMEX Field Campaign, J. Atmos. Sci., 62, 192–206, https://doi.org/10.1175/JAS-3378.1, 2005.

Nair, V. S., Jayachandran, V. N., Kompalli, S. K., Gogoi, M. M., and Babu, S. S.: Cloud condensation nuclei properties of South Asian outflow over the northern Indian Ocean during winter, Atmos. Chem. Phys., 20, 3135–3149, https://doi.org/10.5194/acp-20-3135-2020, 2020.

Nair, V. S., Ajith, T. C., Jayachandran, V. N., Kompalli, S. K., Gogoi, M. M., and Babu, S. S.: Effects of South Asian outflow on aerosol hygroscopicity and cloud droplet activation over the northern Indian Ocean, Atmos. Environ., 327, 120500, https://doi.org/10.1016/j.atmosenv.2024.120500, 2024.

https://doi.org/10.5194/egusphere-2026-842
Preprint. Discussion started: 24 February 2026

O'Dowd, C. D. and de Leeuw, G.: Marine aerosol production: a review of the current knowledge, Phil. Trans. R. Soc. A, 365, 1753–1774, https://doi.org/10.1098/rsta.2007.2043, 2007.

Ou, H., Cai, M., Zhang, Y., Ni, X., Liang, B., Sun, Q., Mai, S., Sun, C., Zhou, S., Wang, H., Sun, J., and Zhao, J.: Measurement report: Cloud condensation nuclei (CCN) activity in the South China Sea from shipborne observations during the summer and winter of 2021 – seasonal variation and anthropogenic influence, Atmos. Chem. Phys., 25, 2495–2513, https://doi.org/10.5194/acp-25-2495-2025, 2025.

Park, C., Soden, B. J., Kramer, R. J., L'Ecuyer, T. S., and He, H.: Observational constraints suggest a smaller effective radiative forcing from aerosol–cloud interactions, Atmos. Chem. Phys., 25, 7299–7313, https://doi.org/10.5194/acp-25-7299-2025, 2025.

Park, J., Dall'Osto, M., Park, K., Gim, Y., Kang, H. J., Jang, E., Park, K.-T., Park, M., Yum, S. S., Jung, J., Lee, B. Y., and Yoon, Y. J.: Shipborne observations reveal contrasting Arctic marine, Arctic terrestrial and Pacific marine aerosol properties, Atmos. Chem. Phys., 20, 5573–5590, https://doi.org/10.5194/acp-20-5573-2020, 2020.

Park, K.-T., Yoon, Y. J., Lee, K., Tunved, P., Krejci, R., Ström, J., Jang, E., Kang, H. J., Jang, S., Park, J., Lee, B. Y., Traversi, R., Becagli, S., and Hermansen, O.: Dimethyl Sulfide-Induced Increase in Cloud Condensation Nuclei in the Arctic Atmosphere, Global Biogeochem. Cy., 35, e2021GB006969, https://doi.org/10.1029/2021GB006969, 2021.

Petters, M. D. and Kreidenweis, S. M.: A single parameter representation of hygroscopic growth and cloud condensation nucleus activity, Atmos. Chem. Phys., 7, 1961–1971, https://doi.org/10.5194/acp-7-1961-2007, 2007.

Quinn, P. K. and Bates, T. S.: The case against climate regulation via oceanic phytoplankton sulphur emissions, Nature, 480, 51–56, https://doi.org/10.1038/nature10580, 2011.

Quinn, P. K., Bates, T. S., Coffman, D. J., Johnson, J. E., and Upchurch, L. M.: Climate Roles of Non-Sea Salt Sulfate and Sea Spray Aerosol in the Atmospheric Marine Boundary Layer: Highlights of 40 Years of PMEL Research, Oceanography, 36, 168–174, https://doi.org/10.5670/oceanog.2023.202, 2023.

Sanchez, K. J., Chen, C.-L., Russell, L. M., Betha, R., Liu, J., Price, D. J., Massoli, P., Ziemba, L. D., Crosbie, E. C., Moore, R. H., Müller, M., Schiller, S. A., Wisthaler, A., Lee, A. K. Y., Quinn, P. K., Bates, T. S., Porter, J., Bell, T. G., Saltzman, E. S.,

https://doi.org/10.5194/egusphere-2026-842
Preprint. Discussion started: 24 February 2026

910 Vaillancourt, R. D., and Behrenfeld, M. J.: Substantial Seasonal Contribution of Observed
911 Biogenic Sulfate Particles to Cloud Condensation Nuclei, Sci. Rep., 8, 3235,
912 https://doi.org/10.1038/s41598-018-21590-9, 2018.

913 Sanchez, K. J., Roberts, G. C., Saliba, G., Russell, L. M., Twohy, C., Reeves, J. M.,
914 Humphries, R. S., Keywood, M. D., Ward, J. P., and McRobert, I. M.: Measurement
915 report: Cloud processes and the transport of biological emissions affect southern ocean
916 particle and cloud condensation nuclei concentrations, Atmos. Chem. Phys., 21, 3427–
917 3446, https://doi.org/10.5194/acp-21-3427-2021, 2021.

918 Seinfeld, J. H. and Pandis, S. N.: Atmospheric Chemistry and Physics: From Air Pollution to
919 Climate Change, 3rd edn., John Wiley & Sons, Hoboken, NJ, USA, ISBN:978-1-118-
920 94740-1, 2016.

921 Stein, A. F., Draxler, R. R., Rolph, G. D., Stunder, B. J. B., Cohen, M. D., and Ngan, F.:
922 NOAA's HYSPLIT Atmospheric Transport and Dispersion Modeling System, B. Am.
923 Meteorol. Soc., 96, 2059–2077, https://doi.org/10.1175/BAMS-D-14-00110.1, 2015.

924 Tatzelt, C., Henning, S., Welti, A., Baccarini, A., Hartmann, M., Gysel-Beer, M., van
925 Pinxteren, M., Modihi, R. L., Schmale, J., and Stratmann, F.: Circum-Antarctic
926 abundance and properties of CCN and INPs, Atmos. Chem. Phys., 22, 9721–9745,
927 https://doi.org/10.5194/acp-22-9721-2022, 2022.

928 Thornton, J. A., Virts, K. S., Holzworth, R. H., and Mitchell, T. P.: Lightning enhancement
929 over major oceanic shipping lanes, Geophys. Res. Lett., 44, 9102–9111,
930 https://doi.org/10.1002/2017GL074982, 2017.

931 Twigg, M. M., Ilyinskaya, E., Beccaceci, S., Green, D. C., Jones, M. R., Langford, B.,
932 Leeson, S. R., Lingard, J. J. N., Pereira, G. M., Carter, H., Poskitt, J., Richter, A., Ritchie,
933 S., Simmons, I., Smith, R. I., Tang, Y. S., Van Dijk, N., Vincent, K., Nemitz, E., Vieno,
934 M., and Braban, C. F.: Impacts of the 2014–2015 Holuhraun eruption on the UK
935 atmosphere, Atmos. Chem. Phys., 16, 11415–11431, https://doi.org/10.5194/acp-16-
936 11415-2016, 2016.

937 Twomey, S.: The nuclei of natural cloud formation part II: The supersaturation in natural
938 clouds and the variation of cloud droplet concentration, Geofis. Pura Appl., 43, 243–249,
939 https://doi.org/10.1007/BF01993560, 1959.

https://doi.org/10.5194/egusphere-2026-842
Preprint. Discussion started: 24 February 2026

940 Twomey, S.: Pollution and the planetary albedo, Atmos. Environ., 8, 1251–1256,
941 https://doi.org/10.1016/0004-6981(74)90004-3, 1974.

942 Twomey, S.: Aerosols, clouds and radiation, Atmos. Environ., 25, 2435–2442,
943 https://doi.org/10.1016/0960-1686(91)90159-5, 1991.

944 Ueda, S., Miura, K., Kawata, R., Furutani, H., Uematsu, M., Omori, Y., and Tanimoto, H.:
945 Number-size distribution of aerosol particles and new particle formation events in tropical
946 and subtropical Pacific Oceans, Atmos. Environ., 142, 324–339,
947 https://doi.org/10.1016/j.atmosenv.2016.07.055, 2016.

948 Wood, R., Wyant, M., Bretherton, C. S., Rémillard, J., Kollias, P., Fletcher, J., Stemmler, J.,
949 de Szoeke, S., Yuter, S., Miller, M., Mechem, D., Tselioudis, G., Chiu, J. C., Mann, J. A.
950 L., O'Connor, E. J., Hogan, R. J., Dong, X., Miller, M., Ghate, V., Jefferson, A., Min, Q.,
951 Minnis, P., Palikonda, R., Albrecht, B., Luke, E., Hannay, C., and Lin, Y.: Clouds,
952 Aerosols, and Precipitation in the Marine Boundary Layer: An ARM Mobile Facility
953 Deployment, B. Am. Meteorol. Soc., 96, 419–440, https://doi.org/10.1175/BAMS-D-13-
954 00180.1, 2015.

955 Yoo, M., Cho, J., Sung, M., Lee, S., Kim, M., Ramu, A. G., Chung, H., Choi, J., Lee, T.,
956 Park, J., and Lee, H.: Aircraft observations of black carbon over the Yellow Sea and
957 Seoul Metropolitan Area: Vertical profiles and air mass origin influence, J. Environ. Sci.,
958 in press, https://doi.org/10.1016/j.jes.2025.10.034, 2025.

959 Zhou, S., Xu, Z., Chen, Y., Zhao, M., Li, Y., and Yan, K.: Anthropogenic air pollutants
960 strongly interact with natural aerosols over the eastern China seas: key processes, size
961 distributions, and seasonalities, Atmos. Chem. Phys., 25, 13597–13619,
962 https://doi.org/10.5194/acp-25-13597-2025, 2025.